Convergence Investigation of Injection-Based Encoderless Control Algorithms for RSMs in Deep Magnetic Saturation

MATTHIAS LAUMANN[1,2], **(Member, IEEE), CHRISTIAN WEINER**[2]**, (Member, IEEE), AND RALPH M. KENNEL**[1]**, (Senior Member, IEEE)**

[1]Institute for Electrical Drive Systems and Power Electronics, Technical University of Munich, 80333 Munich, Germany
[2]Faculty of Electrical Engineering, Darmstadt University of Applied Sciences, 64295 Darmstadt, Germany

Corresponding author: Matthias Laumann (matthias.laumann@h-da.de)

ABSTRACT Injection-based encoderless control methods are the state-of-the-art solution for estimating the rotor position around zero speed. It is known that stability is a major issue in this category of algorithms. Most of these methods become incapable of tracking the rotor position when the machine is driven into deep magnetic saturation. In recent literature, this behavior is often assumed to be a property of the electrical machine. Thus, recent research in this field has focused on the optimization of the electrical machine. The purpose of the following work is to investigate the impact of injection-based encoderless algorithms on the stability issue in deep magnetic saturation. By investigating various algorithms for a reluctance synchronous machine (RSM), it is shown for the first time that the issue results primarily from the algorithm used. One of the investigated algorithms is capable of working without load limitation, confirming the statement that the algorithm is the source of the problem. The reason for this behavior is analyzed using a novel convergence criterion for the RSM, which is derived and verified. A Finite-Element-Method (FEM)-based simulation procedure is proposed to predict the convergence region with high accuracy. This opens new practical relevant possibilities at the design stage of the system. The investigation demonstrates that a deviation between the real and estimated operating point causes the problem. This deviation results in incorrect parameters and thus leads to the instability of the injection-based model.

INDEX TERMS Sensorless control, encoderless control, reluctance synchronous machine, saturation, magnetic anisotropy, stability, load limitation, convergence region, observability, voltage injection.

I. INTRODUCTION

Synchronous machines are a focus of current research due to their high efficiency and robustness. Compared to induction machines, the drawback of these machines is that the rotor angle has to be known for efficient control. This additional requirement results in increased costs for the encoder technology, additional space to mount the sensor, and less reliability due to potential encoder failure. However, this issue can be overcome by applying encoderless control methods. Encoderless control, also called sensorless control, was initially based on electromotive force (EMF) methods e.g. [1], [2]. EMF-based methods use the information included in the

The associate editor coordinating the review of this manuscript and approving it for publication was Binit Lukose.

induced voltage in order to demodulate the rotor angle and rotor speed. However, these methods have a physical limitation caused by the disappearance of the induced voltage near to zero speed. Therefore, injection-based encoderless control methods were developed e.g. [3], [4]. Injection-based methods use the position-dependent differential inductance to demodulate the rotor position. This is commonly implemented by injecting high-frequency voltages and measuring the anisotropy-modulated current derivatives.

Since the first use of these injection-based methods, there have been three major problems preventing their widespread use in industry. The first problem is the additional acoustic noise due to the voltage injection. However, this problem has been overcome as shown in [5]–[8]. The accuracy of the methods, when compared to that of a high-resolution resolver,

TABLE 1. Basic nomenclature and notations.

Dimensions

Symbol	Description
X, x	scalar
$\boldsymbol{x}$	vector
$\boldsymbol{X}$	matrix

Superscript

Symbol	Description
s	quantity in two-phase stator fixed coordinates
r	quantity in rotor fixed coordinates
a	quantity in anisotropy fixed coordinates
-1	inverse matrix, reversed function, or reciprocal
$\top$	transposed matrix or vector
$*$	reference value

Subscripts

Symbol	Description
el	quantity in electrical units
m	quantity in mechanical units
n	nominal value
s	stator related quantity or *sampling* in case of a time
A	parameter related to the magnetic anisotropy
d, q	abscissa and ordinate in rotor coordinates

Accents

Symbol	Description
$\acute{L}$	differential inductance
$\hat{x}$	estimated parameter which might contain an error

Matrices

Symbol	Description
$\mathbf{I}_i$	unity matrix ($\mathbf{I}_i \in \mathbb{R}^i$)
$\boldsymbol{P}(x)$	$\alpha/\beta-$ to d/q$-$ transformation
$\mathbf{C}$	Clarke transformation
$\mathbf{J}$	counterclockwise rotation of $90°$ ($\boldsymbol{P}(-90°)$)

Physical quantities

Symbol	Description
t, T, f	time, time period, and frequency
τ	time constant
u, i	voltage and current
ψ	flux linkage
R, L, Y	resistance, inductance and admittance
θ, ω, p	angle, angular frequency and number of pole pairs
M, n	torque and speed
Γ	stability factor

is the second problem and has yet to be resolved. However, the achievable accuracy is sufficient for most applications. The third problem is the overload capability and the impact of strong harmonic anisotropies. Approaches for compensating the impact of harmonic anisotropies were proposed in [9], [10]. The overload capability problem is yet to be described satisfactorily. The schemes tend to become inaccurate and unstable if the machine is operated in deep magnetic saturation. This excludes the use of this methods for many applications, e.g. in the automotive sector. Thus, recent research in the area of encoderless control focuses on the *overload problem*, which is often also denoted in conjunction with the terminologies *convergence region*, *stability*, and *overload limit*.

The authors of [11] investigated the observability of the induction machine and the synchronous machine for encoderless control, by applying the conventional theory of observability. Their criterion guarantees observability when an EMF-based method is used and without taking parameter deviations into account. However, parameter deviations are not to be neglected when using an injection-based encoderless algorithm as shown in [16]. The authors of [12]–[15] also state that the loss in observability is the cause of the problem. However, some of the limits defined in the papers regarding observability can be overcome by considering saturation effects due to estimation errors. The authors of [16] firstly showed that stability and observability have to be considered separately and introduced three criteria for stable operation. The authors of [16] stated that observability is not sufficient for a stable operation of injection-based encoderless algorithms. The authors considered estimation errors to be the cause of the instability. The criteria presented in the paper are assumed to be identical for the different injection-based algorithms. Thus, stability is determined by the properties of the electrical machine in the opinion of [16]. The authors of [17]–[21] attempted to modify existing and developed new models to increase the convergence region. In [22] it is also shown that temperature can influence the stability behavior as well. Based on the widespread assumption that the overload capability is determined by the machine [16], [23], several approaches have been proposed to optimize the machine to improve its stability properties [12], [13], [24]–[26].

However, the following open questions regarding the overload capability problem are still to be answered:

- Existing convergence criteria developed to predict the convergence region are not reliable for the prediction of the convergence region of different injection-based models. Existing criteria are derived based on an underlying algorithm, which leads to the problem that the derived criterion can only be valid for the injection-based model assumed in the derivation.
- There is no comparison between different existing injection-based methods regarding the overload capability problem. Furthermore, the stability issues are often assumed (but not proofed) to be solely a property of the machine.
- An FEM-based simulation procedure for the prediction of the convergence region, that can be applied to different injection-based algorithms. Such a procedure could be used to verify early in the design stage of the machine, whether the indented combination

of machine and algorithm can achieve the desired torque.

- There is no generally confirmed scientific statement about how to solve the problem. Nevertheless, this is important to develop improved models in the future, that can overcome the overload capability problem.

Following on from the above, the novelty of this paper is the investigation of the impact of the injection-based algorithms on the issue of stability in deep magnetic saturation. The aim is to answer the open questions stated above. Firstly, five different algorithms are investigated by an empirical test regarding their overload capability. Then, from the results of the empirical test, a new stability criterion for the RSM is derived. The experimental verifications of the criterion confirm that it can predict the overload limit of several algorithms. Finally, an FEM-based simulation procedure is proposed, which can precisely predict the convergence region for different injection-based encoderless algorithms.

The results, which are applied to an RSM, show that the overload limit is strongly influenced by the algorithm used. This statement is confirmed by the fact that one of the algorithms investigated functions without becoming unstable at any investigated operating point. The others show strong variations in the overload capability. The investigations give rise to the assumption that deviations in the estimated parameters used in the algorithm are the cause of the overload limit. The deviations in the estimated parameters are caused by the deviation between the real and the assumed operating point of the machine. This behavior is assessed by the new stability criterion.

Frequently used notation and the basic nomenclature in this paper are presented in Table 1. Additional descriptions are introduced in the document.

II. CONVENTIONAL ANISOTROPY MODEL

Injection-based encoderless control algorithms, which are also referred to as anisotropy-based methods, make use of the information included in the current derivatives to estimate rotor speed and angle. As their name implies, most of these methods determine the magnetic anisotropy rather than the actual rotor angle. The anisotropy model is a central element of most methods and is therefore described briefly below. It can be deduced from the voltage equation in the rotor coordinates of the RSM, which is given by:

$$\boldsymbol{u}_{\text{s}}^{\text{r}} = R\, \boldsymbol{i}_{\text{s}}^{\text{r}} + \acute{\boldsymbol{L}}_{\text{s}}^{\text{r}} \frac{\mathrm{d}\boldsymbol{i}_{\text{s}}^{\text{r}}}{\mathrm{d}t} + \omega_{\text{el}} \mathbf{J} \boldsymbol{\psi}_{\text{s}}^{\text{r}} \tag{1}$$

$$\boldsymbol{\psi}_{\text{s}}^{\text{r}} = \begin{bmatrix} L_{\text{d}} & 0 \\ 0 & L_{\text{q}} \end{bmatrix} \boldsymbol{i}_{\text{s}}^{\text{r}} \tag{2}$$

This voltage equation neglects the capacitive behavior of the machine, the effect of iron losses, leakage inductances, and higher flux linkage harmonics. To allow for the effect of cross saturation, the inductance matrix in rotor coordinates includes

the coupling elements ($\acute{\boldsymbol{L}}_{\text{s}}^{\text{r}} = \acute{\boldsymbol{L}}_{\text{s}}^{\text{r}^{\top}}$; $\boldsymbol{x}^{\top} \acute{\boldsymbol{L}}_{\text{s}}^{\text{r}} \boldsymbol{x} \geq 0, \forall \boldsymbol{x} \in \mathbb{R}^2$).

$$\acute{\boldsymbol{L}}_{\text{s}}^{\text{r}} = \begin{bmatrix} \dfrac{\partial \psi_{\text{d}}}{\partial i_{\text{d}}} & \dfrac{\partial \psi_{\text{d}}}{\partial i_{\text{q}}} \\[2mm] \dfrac{\partial \psi_{\text{q}}}{\partial i_{\text{d}}} & \dfrac{\partial \psi_{\text{q}}}{\partial i_{\text{q}}} \end{bmatrix} = \begin{bmatrix} \acute{L}_{\text{dd}} & \acute{L}_{\text{dq}} \\ \acute{L}_{\text{qd}} & \acute{L}_{\text{qq}} \end{bmatrix} \tag{3}$$

$\acute{L}_{\text{dd}}$ and $\acute{L}_{\text{qq}}$ are the differential inductances of the d- and q-axis and $\acute{L}_{\text{dq}}$ is the cross saturation inductance. The voltage equation in stator coordinates can be found by applying the inverse Park transformation to (1), which results in:

$$\boldsymbol{u}_{\text{s}}^{\text{s}} = R\, \boldsymbol{i}_{\text{s}}^{\text{s}} + \acute{\boldsymbol{L}}_{\text{s}}^{\text{s}} \frac{\mathrm{d}\boldsymbol{i}_{\text{s}}^{\text{s}}}{\mathrm{d}t} + \omega_{\text{el}} \left(\mathbf{J} \boldsymbol{\psi}_{\text{s}}^{\text{s}} - \acute{\boldsymbol{L}}_{\text{s}}^{\text{s}} \mathbf{J} \boldsymbol{i}_{\text{s}}^{\text{s}} \right) \tag{4}$$

where the inductance matrix in stator coordinates is described by:

$$\acute{\boldsymbol{L}}_{\text{s}}^{\text{s}} = \acute{L}_{\Sigma} \mathbf{I}_2 + \acute{L}_{\Delta} \boldsymbol{S}(\theta_{\text{el}}) - \acute{L}_{\text{dq}} \boldsymbol{S}(\theta_{\text{el}}) \mathbf{J} \tag{5}$$

$$\acute{L}_{\Sigma} = \frac{\acute{L}_{\text{dd}} + \acute{L}_{\text{qq}}}{2} \tag{6}$$

$$\acute{L}_{\Delta} = \frac{\acute{L}_{\text{dd}} - \acute{L}_{\text{qq}}}{2} \tag{7}$$

$$\boldsymbol{S}(\theta_{\text{el}}) = \begin{bmatrix} \cos(2\theta_{\text{el}}) & \sin(2\theta_{\text{el}}) \\ \sin(2\theta_{\text{el}}) & -\cos(2\theta_{\text{el}}) \end{bmatrix} \tag{8}$$

This inductance matrix can be further compacted using the harmonic addition theorem, resulting in only one angle-dependent term:

$$\acute{\boldsymbol{L}}_{\text{s}}^{\text{s}} = \acute{L}_{\Sigma} \mathbf{I}_2 + \acute{L}_{\text{A}}\, \boldsymbol{S}(\theta_{\text{A}}) \tag{9}$$

$$\acute{L}_{\text{A}} = \sqrt{\acute{L}_{\Delta}^2 + \acute{L}_{\text{dq}}^2} \tag{10}$$

$$\theta_{\text{A}} = \theta_{\text{el}} + \frac{1}{2} \arctan\left(\frac{\acute{L}_{\text{dq}}}{\acute{L}_{\Delta}} \right) = \theta_{\text{el}} + \theta_{\delta} \tag{11}$$

Equation (9) describes the magnetic anisotropy with θ_{A} being the so-called anisotropy angle. This anisotropy angle (11) depends on the actual rotor angle θ_{el} as well as on the misalignment angle θ_{δ}, which describes the shift in angle due to magnetic saturation.

Anisotropy methods have in common that they work based on the principle of injecting a voltage with frequencies higher than the fundamental voltage and evaluating the anisotropy-angle-modulated current derivatives. If the frequency of the injected voltage $\boldsymbol{u}_{\text{s,inj}}^{\text{s}}$ is chosen sufficiently high, the relationship between the voltage and the current derivative simplifies to:

$$\frac{\mathrm{d}\boldsymbol{i}_{\text{s}}^{\text{s}}}{\mathrm{d}t} \approx \left(\acute{\boldsymbol{L}}_{\text{s}}^{\text{s}} \right)^{-1} \boldsymbol{u}_{\text{s,inj}}^{\text{s}} \tag{12}$$

where the inverse inductance is often referred to as the admittance $\acute{\boldsymbol{Y}}_{\text{s}}^{\text{s}}$. This is done to improve the clarity and comprehensibility of the mathematical description.

$$\left(\acute{\boldsymbol{L}}_{\text{s}}^{\text{s}} \right)^{-1} = \acute{\boldsymbol{Y}}_{\text{s}}^{\text{s}} = \acute{Y}_{\Sigma} \mathbf{I}_2 + \acute{Y}_{\text{A}} \boldsymbol{S}(\theta_{\text{A}}) \tag{13}$$

$$\acute{Y}_\Sigma = \frac{-\acute{L}_\Sigma}{\hat{L}_A^2 - \acute{L}_\Sigma^2} \qquad (14)$$

$$\acute{Y}_A = \frac{\acute{L}_A}{\hat{L}_A^2 - \acute{L}_\Sigma^2} \qquad (15)$$

At the end, it should be registered that the rotor angle differs from the anisotropy angle in a manner that depends on the operating point, as shown in (11). This is a result of magnetic saturation and leads to the problem that the actual rotor angle cannot be determined directly using such a conventional model. Therefore, most algorithms make use of a second algorithm, which compensates for the term $\theta_\delta = f(i_s^r)$ of equation (11). This second algorithm is often referred to as the rotor angle assignment algorithm.

III. CONVENTIONAL ROTOR ANGLE ASSIGNMENT
The purpose of the rotor angle assignment algorithm is to determine the real rotor angle θ_{el} from the measured anisotropy angle θ_A (or from a vector related to the anisotropy) using knowledge of the actual estimated or assumed operating point $(\hat{i}_s^r)$. For the purposes of this paper, it is not important to describe this rotor angle assignment algorithm in detail. Many such algorithms exist e.g. [9], [10], which all have their own scope of application. However, all of these conventional algorithms rely on the estimated operating point $(\hat{i}_s^r)$ of the machine to be able to estimate the actual term $\theta_\delta = f(i_s^r)$. It will be shown, that the use of an estimated or assumed operating point is one of the reasons why conventional injection-based algorithms can become unstable when operating an RSM. The terminology ''*conventional*'' is used in the following to refer to the category of algorithms that rely on an estimated or assumed operating-point-dependent rotor angle assignment. It should be noted that there are numerous implementation versions of such a rotor angle assignment algorithm. However, the algorithm used in this investigation considers the misalignment angle as a function of the current amplitude (along the maximum torque per ampere (MTPA) trajectory) $\hat{\theta}_\delta = f(\left|i_{s,MTPA}^s\right|)$ only. This is probably the most common and simple way of implementing this algorithm.

IV. ENCODERLESS MODELS
In the following section, four different injection-based models are discussed. Each model has different properties and needs to be implemented differently. By investigating different algorithms it is possible to assess whether the overload capability is dependent on the algorithm used as asserted in the introduction. All algorithms are state of the art and therefore not discussed in detail. However, the necessary equations are briefly discussed to make the results of this work interpretable. The detailed derivations of the models can be found in the given references, which are mentioned in each subsection.
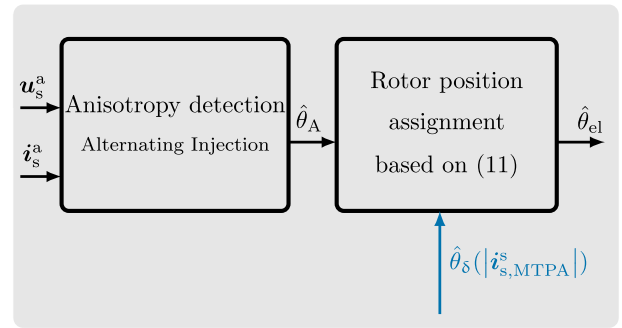

FIGURE 1. Conventional structure of Alternating Injection.

A. ALTERNATING INJECTION
The algorithm based on the Alternating Injection [4], [27] model utilizes the current response of the machine to a high-frequency ω_c sinusoidal voltage injection with amplitude $\tilde{u}_c$ into the estimated anisotropy d-axis. The aim is to control the angle in such a way, that the high-frequency current response along the anisotropy q-axis $i_{A,q}$ disappears. Without the presence of cross saturation, this could be used to directly determine the rotor position. It should be noted, that the convergence of the estimated anisotropy angle towards the actual one does not depend on model parameters. The final equation, which is used for the estimation can be derived from (12). Equation (12) is first transformed into so-called anisotropy coordinates. The transformation from stator into anisotropy coordinates x_s^a can be performed using the Park transformation $P(\theta_A)$ with the anisotropy angle as the argument. The final anisotropy angle estimation is based on the measured anisotropy q-axis current response. According to [28, p. 956], it is given by:

$$i_{A,q} = \frac{-2\acute{Y}_A\tilde{u}_c}{\omega_c}\left(\hat{\theta}_A - \theta_A\right) \qquad (16)$$

The estimation equation (16) is dependent on $\acute{Y}_A$, which is unknown. This aggravates the tuning of the tracking type filter. Fig. 1 shows the basic structure of common Alternating Injection, consisting of anisotropy detection and rotor position assignment.

B. CONVENTIONAL ARBITRARY INJECTION-BASED MODEL
The model based on the conventional Arbitrary Injection approach was first proposed about a decade ago [29], [30] and is discussed in detail in [31]. The aim was to make the encoderless control method independent of the shape of the voltage injection and any filtering. The fundamental behavior (frequency ω_{el}) of the machine is eliminated by measuring multiple current and voltage instances. With the assumption of a constant or linearly changing fundamental behavior of the machine over the measuring instances, the high-frequency behavior can be isolated. In this case, the general approach (12) is discretized and adopted based on [32],
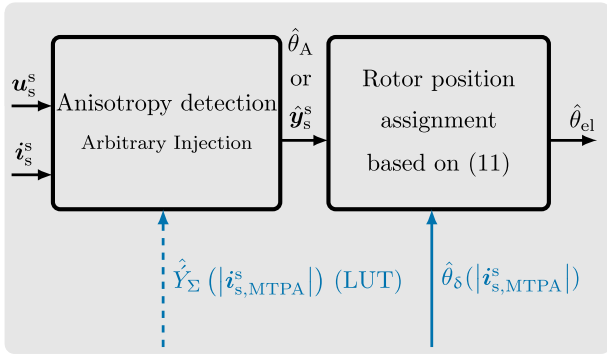
FIGURE 2. Conventional structures of Arbitrary Injection.

which yields:

$$\frac{\Delta^2 \boldsymbol{i}_\mathrm{s}^\mathrm{s}[k]}{T_\mathrm{s}} = \left(\acute{Y}_\Sigma \mathbf{I}_2 + \acute{Y}_\mathrm{A} \boldsymbol{S}(\theta_\mathrm{A}) \right) \Delta^2 \boldsymbol{u}_\mathrm{s}^\mathrm{s}[k-1] \qquad (17)$$

with

$$\Delta^2 \boldsymbol{i}_\mathrm{s}^\mathrm{s}[k] = \left(\boldsymbol{i}_\mathrm{s}^\mathrm{s}[k] - \boldsymbol{i}_\mathrm{s}^\mathrm{s}[k-1] \right) - 2 \left(\boldsymbol{i}_\mathrm{s}^\mathrm{s}[k-1] - \boldsymbol{i}_\mathrm{s}^\mathrm{s}[k-2] \right) \ldots$$
$$\ldots + \left(\boldsymbol{i}_\mathrm{s}^\mathrm{s}[k-2] - \boldsymbol{i}_\mathrm{s}^\mathrm{s}[k-3] \right) \qquad (18)$$

$$\Delta^2 \boldsymbol{u}_\mathrm{s}^\mathrm{s}[k-1] = \boldsymbol{u}_\mathrm{s}^\mathrm{s}[k-1] - 2\boldsymbol{u}_\mathrm{s}^\mathrm{s}[k-2] + \boldsymbol{u}_\mathrm{s}^\mathrm{s}[k-3] \qquad (19)$$

when the so-called delta-squared-version [31, p. 39] is used. Here, T_s is the sampling time, and $[k]$ indicates the current sampling instance, whereas $[k-1]$ denotes the predecessor sampling instance. However, (17) cannot be used directly to determine the anisotropy angle because it includes a non-angle-dependent term scaling with the mean admittance $\acute{Y}_\Sigma$. This term must first be subtracted to obtain the final estimation equation:

$$\acute{Y}_\mathrm{A} \boldsymbol{S}(\theta_\mathrm{A}) \Delta^2 \boldsymbol{u}_\mathrm{s}^\mathrm{s}[k-1] = \frac{\Delta^2 \boldsymbol{i}_\mathrm{s}^\mathrm{s}[k]}{T_\mathrm{s}} - \acute{Y}_\Sigma \mathbf{I}_2 \Delta^2 \boldsymbol{u}_\mathrm{s}^\mathrm{s}[k-1] \quad (20)$$

The estimation vector (20) includes two unknowns $\acute{Y}_\mathrm{A}$ and θ_A, which can be estimated using the two equations of (20). The model benefits from the fact that it does not rely on filtering and that it is almost independent of the shape of the injection voltage. The drawback of this method is that the mean admittance component $\acute{Y}_\Sigma$ must be known. However, it can be pre-determined and stored in a lookup table (LUT). It can also be determined online using the approaches presented in [33], [34]. The stability behavior of the Arbitrary Injection model will be investigated for both approaches for estimating the mean admittance $\acute{Y}_\Sigma$.

C. MODEL IN STATOR COORDINATES
The model depicted below has yet to be referred to in research-related literature, however, it is discussed in detail and introduced in patent [35]. The authors of the patent suspected feedback, which arise when parameters based on the d-q-reference frame are used, to be the cause of the

divergence problem. The patent introduces the idea of decoupling the rotor position assignment algorithm from the estimated operating point. Instead, the rotor position assignment algorithm is fed with the measurable and therefore known currents in stator coordinates. However, the first algorithm used to estimate the anisotropy is still based on a conventional method, although it needs to be executed in stator coordinates only. The previously described Arbitrary Injection method with online estimation of the mean admittance could be used as an anisotropy detection algorithm. The main principle of the method is briefly discussed below. For a detailed description, refer to [35]. The anisotropy vector in stator coordinates $\boldsymbol{y}_\mathrm{s}^\mathrm{s}$ is commonly described as a function of the currents in the rotor fixed reference frame and the rotor angle

$$\boldsymbol{y}_\mathrm{s}^\mathrm{s} = \boldsymbol{f} \left(\boldsymbol{i}_\mathrm{s}^\mathrm{r}, \theta_\mathrm{el} \right). \qquad (21)$$

The anisotropy vector $\boldsymbol{y}_\mathrm{s}^\mathrm{s}$ can be constructed using the four possible linear combinations of the admittance matrix [35] in stator coordinates:

$$\acute{\boldsymbol{Y}}_\mathrm{s}^\mathrm{s} = \begin{bmatrix} \acute{Y}_{\alpha\alpha} & \acute{Y}_{\alpha\beta} \\ \acute{Y}_{\beta\alpha} & \acute{Y}_{\beta\beta} \end{bmatrix} = \acute{Y}_\Sigma \mathbf{I}_2 + \acute{Y}_\mathrm{A} \boldsymbol{S}(\theta_\mathrm{A}) \qquad (22)$$

whereas the anisotropy vector in this work is constructed from the following two linear combinations:

$$\boldsymbol{y}_\mathrm{s}^\mathrm{s} = \frac{1}{2} \begin{bmatrix} \acute{Y}_{\alpha\alpha} - \acute{Y}_{\beta\beta} \\ \acute{Y}_{\alpha\beta} + \acute{Y}_{\beta\alpha} \end{bmatrix} \qquad (23)$$

It is well-known, that (21) is not always reversible over θ_el (at a fixed current pair) for machines with strong harmonic anisotropies. However, instead of the currents in the rotor fixed reference frame, it can also be described as a function of the currents in the stator fixed reference frame (24). According to [35], the trajectories are monotone over the rotor angle (except at zero current for the RSM) in this case $\left(\boldsymbol{y}_\mathrm{s}^\mathrm{s}(\theta_\mathrm{el}) : \mathbb{R} \to \mathbb{R}^2, \forall \boldsymbol{i}_\mathrm{s}^\mathrm{s} \right)$:

$$\boldsymbol{y}_\mathrm{s}^\mathrm{s} = \boldsymbol{f}_{\left(\boldsymbol{i}_\mathrm{s}^\mathrm{s}, \theta_\mathrm{el} \right) \to \boldsymbol{y}_\mathrm{s}^\mathrm{s}} \left(\boldsymbol{i}_\mathrm{s}^\mathrm{s}, \theta_\mathrm{el} \right) \qquad (24)$$

The basic aim of [35] is to reverse the model (24) in such a way that the rotor position can be found as a function of the anisotropy vector and the currents in stator coordinates:

$$\theta_\mathrm{el} = f_{\left(\boldsymbol{i}_\mathrm{s}^\mathrm{s}, \boldsymbol{y}_\mathrm{s}^\mathrm{s} \right) \to \theta_\mathrm{el}} \left(\boldsymbol{i}_\mathrm{s}^\mathrm{s}, \boldsymbol{y}_\mathrm{s}^\mathrm{s} \right) \qquad (25)$$

This model benefits from the fact that it relies on measurable quantities only and no estimated parameters are used. Furthermore, it can also use multiple rotor-angle-dependent admittance components for the estimation. This allows estimation even if the anisotropy angle does not correlate with the actual rotor angle anymore. However, the complexity of the trajectories of (24) is one of the drawbacks according to [35]. Furthermore, additional measurements are needed in order to derive the relationship $\boldsymbol{y}_\mathrm{s}^\mathrm{s} = \boldsymbol{f}_{\left(\boldsymbol{i}_\mathrm{s}^\mathrm{s}, \theta_\mathrm{el} \right) \to \boldsymbol{y}_\mathrm{s}^\mathrm{s}} \left(\boldsymbol{i}_\mathrm{s}^\mathrm{s}, \theta_\mathrm{el} \right)$. Fig. 3 shows the basic structure of this method.
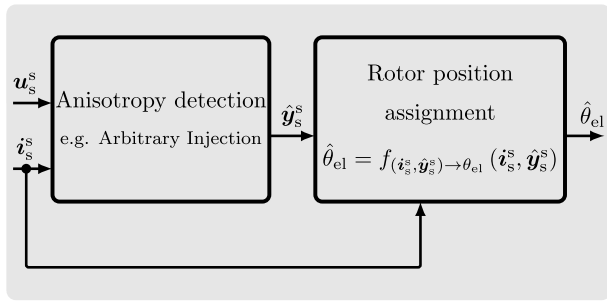
FIGURE 3. Structure according to [35] without any feedback of estimated quantities.
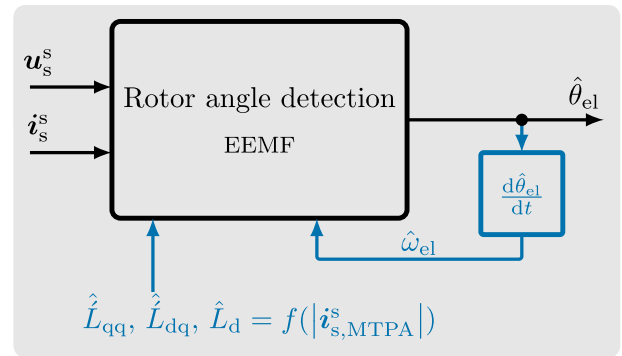

FIGURE 4. Structure of the EEMF.

D. EXTENDED ELECTROMOTIVE FORCE MODEL

The model based on the extended electromotive force (EEMF) [36], [37] was initially introduced for encoderless control of interior permanent magnet synchronous machines (IPMSMs) in the medium to high-speed range and not for application close to a standstill. However, the authors of [38], [39] recognized that it can also be used close to and at a standstill with additional voltage injection. The model estimates the extended electromotive force (EEMF) $e_{s,EEMF}^s$. The estimated EEMF is finally used to determine the estimated rotor angle $\hat{\theta}_{el}$. The authors of the present work propose the extension of the equations presented in [36], [37] by the cross saturation inductance $\acute{L}_{dq}$, which yields:

$$e_{s,EEMF}^s = e_{EEMF} \begin{bmatrix} \cos(\theta_{el}) \\ \sin(\theta_{el}) \end{bmatrix} \tag{26}$$

$$= u_s^s - R\,i_s^s - \acute{L}_{s,EEMF}^s \frac{di_s^s}{dt} \dots$$
$$\dots - \hat{\omega}_{el} \left(L_{s,EEMF}^s - \acute{L}_{s,EEMF}^s \mathbf{J} \right) i_s^s \tag{27}$$

with

$$e_{EEMF} = \omega_{el}\,i_q\,(L_d - L_q) + \frac{di_d}{dt} \left(\acute{L}_{dd} - \acute{L}_{qq} \right) \dots$$
$$\dots + 2\acute{L}_{dq} \frac{di_q}{dt} \tag{28}$$

$$L_{s,EEMF}^s = \begin{bmatrix} 0 & -L_d \\ L_d & 0 \end{bmatrix} \tag{29}$$

$$\acute{L}_{s,EEMF}^s = \begin{bmatrix} \acute{L}_{qq} & -\acute{L}_{dq} \\ \acute{L}_{dq} & \acute{L}_{qq} \end{bmatrix} \tag{30}$$

The current derivatives included in (28) can be excited using an additional voltage injection to enable rotor position estimation close to a standstill. In the present work, a sinusoidal voltage injection in the estimated d-axis is used. The model can be used to directly estimate the rotor angle, without using a second rotor position assignment algorithm. This circumstance and the resulting entirely different structure of the model is the reason why the authors decided to investigate its overload capability. The model relies on many more estimated parameters than the other models. Fig. 4 shows the basic structure of the EEMF based model without a rotor position assignment algorithm.

## V. GENERAL DESCRIPTION OF THE OVERLOAD CAPABILITY PROBLEM

Aside from the loss of general observability [12]–[14] a second phenomenon leads to instability of injection-based methods in deep magnetic saturation. The reason for the phenomenon is estimation errors $\theta_\Delta = \hat{\theta}_{el} - \theta_{el}$ that are encountered during operation in deep magnetic saturation, as explained in [16].

Estimation errors consequently lead to a wrongly rotated voltage vector and thus wrongly rotated current vector if the estimated angle is used in field-oriented control (FOC). The rotated current vector leads to a different magnetic saturation of the machine, which can subsequently lead to a greater or smaller estimation error. The stability criterion of [16] was used in an analysis of this effect. However, only the impact on the conventional rotor position assignment algorithm was analyzed. The influence on further estimated parameters, used by the models, is not considered there. Thus, the criterion of [16] is assumed to describe the stability behavior of Alternating Injection well because Alternating Injection only uses estimated parameters in the rotor position assignment. The following investigations are performed with the aim of understanding and assessing models with structures other than the one analyzed in [16].

VI. EMPIRICAL TEST

In the following section, the overload capability of the different models is investigated and compared. This investigation is performed to obtain an impression of the performance of each model. The results are used to reach general conclusions about the overload issue. The investigation is based on the tests described below.

The RSM with the nominal data provided in Table 2 is subjected to the tests. The RSM is operated on the test bench with the control system shown in Fig. 5 b). Fig. 5 b) shows the basic control structure of the current control loop when field-oriented control is applied. The reference currents are generated from the reference torque by means
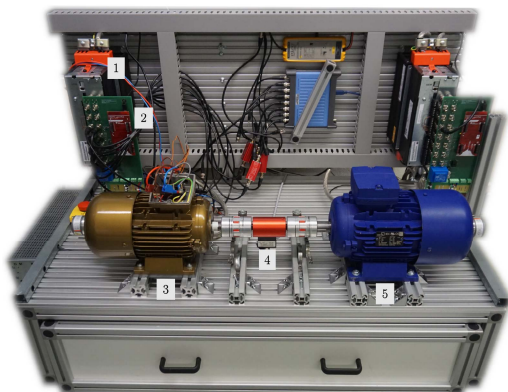
(a) Test bench. **1** modified SEW MDX61B0110-5A3-4-0T inverter **2** microcontroller board based on TI TMS320F2837xS **3** RSM **4** shaft torque measurement **5** load machine.
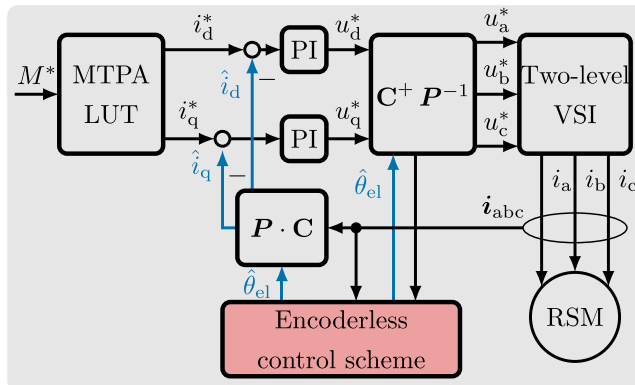
(b) Schematic of the current control structure during closed-loop encoderless operation.

FIGURE 5. Overview of the system used.

TABLE 2. Data of the RSM.

Type KSB 01633731		
Parameter	**Value**	**Description**
I_{N}	4 A	nominal current
M_{N}	9.6 Nm	nominal torque
n_{N}	1500 rpm	nominal mechanical speed
p	2	number of pole pairs
$\acute{L}_{\mathrm{dd}}$	145 mH	at nominal torque (MTPA)
$\acute{L}_{\mathrm{qq}}$	32 mH	at nominal torque (MTPA)
$\acute{L}_{\mathrm{dq}}$	± 8 mH	at nominal torque (MTPA)

FIGURE 6. MTPA trajectory of the RSM up to 41 Nm.

of two LUT. The generated reference currents are regarding the MTPA trajectory. The control errors of the currents are fed to two PI controllers, which adjust the reference voltages to decrease the control errors. The time constants of the current control loops, which are first-order elements (machine time constants compensated), are both set to 2 ms. The reference voltages from the PI controllers are applied to the machine using the space vector modulation and the two-level voltage source inverter (VSI). The measured currents of the rotor fixed reference frame, which are compared with the reference currents, are calculated using the Park transformation $\boldsymbol{P}$ and Clarke transformation $\mathbf{C}$. In the case of an encoderless closed-loop control using the estimated rotor position, the Park transformation and its inverse are fed with the estimated rotor angle $\hat{\theta}_{\mathrm{el}}$. The estimated rotor angle is calculated by the specific model, which is implemented in the block "*encoderless control scheme*". It should be noticed that the RSM has a low harmonic content in the anisotropy, the anisotropy angle is always reversible over the rotor angle, therefore $\left(\theta_{\mathrm{A}}(\theta_{\mathrm{el}}) : \mathbb{R} \rightarrow \mathbb{R}, \forall \, \boldsymbol{i}_{\mathrm{s}}^{r}\right)$. Thus, general observability of the rotor angle can be assumed according to [16]. The injection amplitudes are chosen to be sufficiently high to ensure that the anisotropy-modulated current derivatives can be measured at
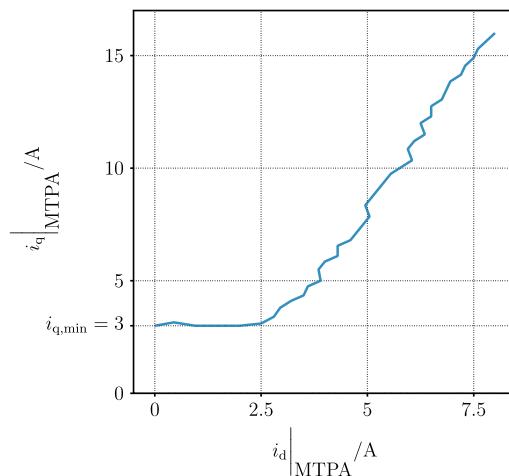
any operating point. A clear assignment of the reason for the instability to the estimation error, which is intended to be investigated in this work, is therefore possible.

Control is implemented using a standard microcontroller, which sends the control commands to a two-level VSI. All the models introduced previously were implemented using this platform. The offline parameters were all pre-determined and stored in an LUT with the same quality for each algorithm. The Arbitrary Injection model was implemented and tested twice, once with the online estimation of $\acute{Y}_{\Sigma}$ according to [33], [34] and once with $\acute{Y}_{\Sigma}$ being pre-determined and stored in an LUT. For the schemes, which rely on the conventional rotor position assignment algorithm described in Section III, the estimated misalignment angle was stored as a function of the current amplitude only. Consequently, the machine is assumed to work along the MTPA trajectory, for which the misalignment term θ_{δ} was measured and the current amplitude $|\hat{\boldsymbol{i}}_{\mathrm{s}}^{\mathrm{s}}|$ is thus referred to. The relation $\hat{\theta}_{\delta} = f(|\hat{\boldsymbol{i}}_{\mathrm{s}}^{\mathrm{s}}|)$

(a) PLL time constant of $\tau_{\mathrm{PLL}} = 16\,\mathrm{ms}$.

(b) PLL time constant of $\tau_{\mathrm{PLL}} = 7\,\mathrm{ms}$.
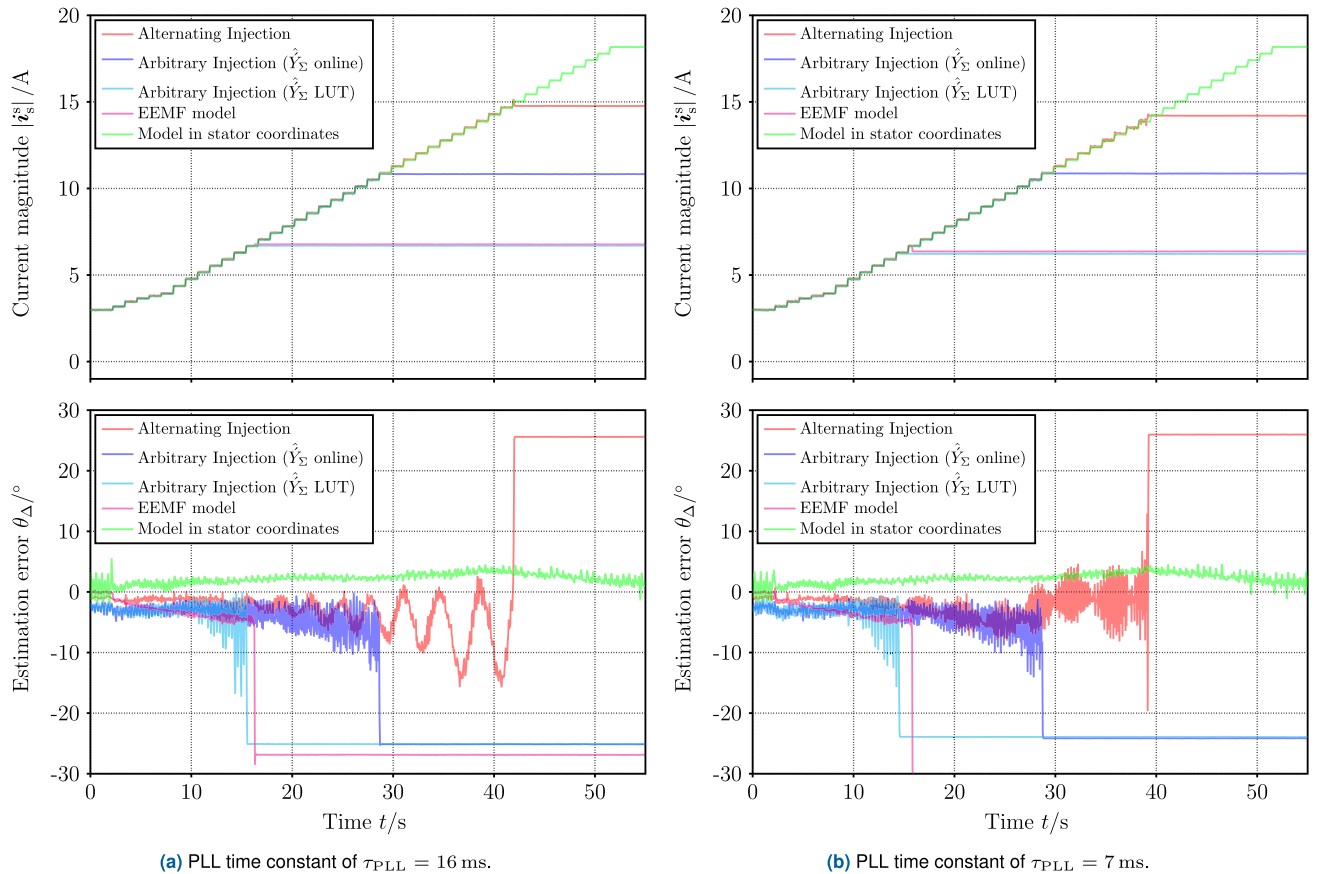
FIGURE 7. Overload test of the different models at an electrical speed of $n_{\mathrm{el}} = 100\,\mathrm{rpm}$.

is implemented using the structure presented in [31, p. 109]. The MTPA trajectory used is shown in Fig. 6. It should be noted that the q-axis current of the trajectory is limited to a minimum of 3 A in order to maintain the saliency of the machine visible. The final estimation equation used to estimate the rotor position is fed to a phase-locked loop (PLL) structure, which is tuned according to the approach presented in [40]. The resulting gains of the PLL are shown below.

The investigation is performed as follows. The RSM is driven in closed-loop current control mode (using the estimated speed and rotor angle), while its rotor speed is held constant at $n_{\mathrm{el}} = 100\,\mathrm{rpm}$ by a load machine. The torque command of the RSM is increased in steps and the estimation error $\theta_{\Delta} = \hat{\theta}_{\mathrm{el}} - \theta_{\mathrm{el}}$ as well as the current amplitude $|\boldsymbol{i}_{\mathrm{s}}^{\mathrm{s}}|$ are monitored. The increase in the current amplitude (reference torque) is timed in such a way that each current amplitude is applied while the rotor passes the entire range of 360°. This ensures, that each rotor angle is covered. The entire control is switched off if $|\theta_{\Delta}| > 25°$ applies and the recent values are hold. If this maximum allowed deviation is reached, this point is taken to be the overload limit of the specific algorithm. This value is chosen based on experience. Experience has shown that the encoderless control algorithm does not find any stable

equilibrium once this limit has been exceeded. In any case, the FOC would be disrupted if such a large estimation error occurred.

Each method is tested twice, once for a PLL time constant of $\tau_{\mathrm{PLL}} = 16\,\mathrm{ms}$ and once for a low time constant of $\tau_{\mathrm{PLL}} = 7\,\mathrm{ms}$ in order to investigate the impact of the PLL as well. This results in a gain of $k_{\mathrm{p,7ms}} = 286\,\mathrm{s}^{-1}$ for the proportional term and a gain of $k_{\mathrm{i,7ms}} = 20000\,\mathrm{s}^{-2}$ for the term of the integrator when a time constant of 7 ms is intended. In the case of a time constant of 16 ms the gains are $k_{\mathrm{p,16ms}} = 125\,\mathrm{s}^{-1}$ and $k_{\mathrm{i,16ms}} = 3900\,\mathrm{s}^{-2}$. Equation (16) states that the gain of the PLL changes with the operating point when Alternating Injection is used. This additional gain is compensated for Alternating Injection by use of the evolved parameters at the operating point of zero reference torque. The results of the investigation are shown in Fig. 7.

The quality criterion of this test is the maximum current amplitude $|\boldsymbol{i}_{\mathrm{s}}^{\mathrm{s}}|_{\mathrm{max}}$ reached before $|\theta_{\Delta}| > 25°$ applies. The measurements show strong variations for this quality measure. The results are assessed in the following, starting with the method with the highest overload capability and continuing to the method with the lowest overload capability.

The maximum current amplitude was reached by the model in stator coordinates described in IV-C with the results in

Fig. 7 (green). The scheme remained stable, even at the maximum current amplitude that can be applied on the test bench. The estimation error remains very small over the entire test.

The Alternating Injection of subsection (IV-A) achieved the second-highest current amplitude; its results are shown in Fig. 7 (red). It reached a maximum current amplitude of $|\boldsymbol{i}_s^s|_{max} = 14.7\,\mathrm{A}$ for $\tau_{PLL} = 16\,\mathrm{ms}$ and $|\boldsymbol{i}_s^s|_{max} = 14.3\,\mathrm{A}$ for $\tau_{PLL} = 7\,\mathrm{ms}$. The measurements reveal that the estimation error increases with the current amplitude. Furthermore, the method is dependent on the PLL settings. The settings have less influence on $|\boldsymbol{i}_s^s|_{max}$, but more on the estimation quality in general. This can be explained based on the operating-point-dependent gain, as it is evident from (16).

The results of the Arbitrary Injection (IV-B) with online admittance estimation are shown in Fig. 7 (blue). The algorithm achieves the same maximum current amplitude of $|\boldsymbol{i}_s^s|_{max} = 10.8\,\mathrm{A}$ for both PLL settings. Its behavior seems to be almost independent on the tracking type filter setup. However, it also shows an increasing estimation error with increasing current amplitude.

The results of the Arbitrary Injection (IV-B) with LUT-based admittance estimation are shown in Fig. 7 (cyan). It achieves a significantly reduced current amplitude than with the online estimation, $|\boldsymbol{i}_s^s|_{max} = 6.7\,\mathrm{A}$ for $\tau_{PLL} = 16\,\mathrm{ms}$ and $|\boldsymbol{i}_s^s|_{max} = 6.3\,\mathrm{A}$ for $\tau_{PLL} = 7\,\mathrm{ms}$. The estimation error increases with the current amplitude as well.

The measurement results of the EEMF based model (IV-D) are presented in Fig. 7 (magenta). It achieves $|\boldsymbol{i}_s^s|_{max} = 6.8\,\mathrm{A}$ for $\tau_{PLL} = 16\,\mathrm{ms}$ and $|\boldsymbol{i}_s^s|_{max} = 6.7\,\mathrm{A}$ for $\tau_{PLL} = 7\,\mathrm{ms}$, almost independent of the PLL setup. This method exhibits a really low noise content in the estimation over the entire test. Nevertheless, the estimation error increases as the current amplitude is increased.

The following conclusions can be reached based on the tests of this section:

- The maximum achievable current amplitude $|\boldsymbol{i}_s^s|_{max}$ is less impacted by the PLL settings, as long as the provided gain factors are meaningfully adapted to the given system and its noise content.
- Small differences in the implementation can make a big difference in the maximum achievable current amplitude, as the implementation versions of the Arbitrary Injection illustrate.
- An assessment based on a stability criterion as proposed in [16] does not ensure success in respect of the prediction of the overload capability of all models. Each performed very differently and the criterion of [16] would have given the same prediction for all models.
- It can be deduced that the overload capability of an RSM is strongly influenced by the encoderless algorithm applied.
- By comparing the maximum achievable current amplitude $|\boldsymbol{i}_s^s|_{max}$ with the structures of the different models, it appears that the more estimated parameters there

are in the algorithm, the less $|\boldsymbol{i}_s^s|_{max}$ will be. This is because the estimated parameters become inaccurate if the machine is not operated on the intended trajectory or at the estimated operating point. The method of (IV-C) confirms this conclusion because it was stable at all operating points and it does not rely on estimated parameters at all.

The findings of this section are utilized for further investigations. This is done theoretically in the following section by deriving a new stability criterion.

VII. CONVERGENCE CRITERION

The measurements in the previous section have shown, that each algorithm performs very differently in deep magnetic saturation. Therefore, criteria that are based on the analysis of a single model, as proposed in the recent literature cannot conclusively explain the results above.

To address this problem, a new and more general stability criterion for the RSM is derived in the following. A deviation between the estimated and real operating point is considered to be the source of the problem. Consequently, the terminology "*operation point*" is used to name all input variables on which the parameters of the specific model are dependent. The deviation between the operating points causes deviations of the estimated parameters. The deviations of the parameters can either lead to a greater or lower estimation error. For most injection-based methods applied to an RSM it can be assumed that the operating point is mainly defined by currents. Thus, the current vector deviation, which is the difference between the actual and estimated current vector, can be assumed to be the cause of the problem. Since the current amplitude is always known, the entire deviation results solely from the deviation in the current angle. Therefore, the dependency of the estimation error on the current angle deviation (where "*current angle*" refers to the angle that defines the direction of the vector of the current and not the currently existing angle) needs to be assessed by a stability criterion in order to guarantee convergence of the estimation error.

The deviation between the current angles can be defined as follows:

$$\theta_{\Delta,i} = \theta_i - \hat{\theta}_i \tag{31}$$

These angles are related to the d-q-reference frame (or another unknown rotating reference frame used to store the required model parameters). With θ_i being the actual current angle. $\hat{\theta}_i$ is the estimated current angle that is used to determine the parameters of the encoderless model or on which the parameters are based. It is of interest for the stability assessment, how the estimation error of the rotor angle develops dependent on the current angle deviation. Thus, the dependency of the rotor angle error $\theta_\Delta = \hat{\theta}_{el} - \theta_{el}$ on the current angle deviation $\theta_{\Delta,i}$ is of interest. Here $\hat{\theta}_{el}$ is the estimated angle of the specific model, considering all its specificities. The relation between the angles can be approximated by a first-order MacLaurin polynomial under

the assumption of small $\theta_{\Delta,\text{i}}$ and θ_Δ being differentiable over $\theta_{\Delta,\text{i}}$ at any operating point. This yields:

$$\theta_\Delta \approx \theta_\Delta \Big|_{\theta_{\Delta,\text{i}}=0°} + \theta_{\Delta,\text{i}} \cdot \frac{\partial \theta_\Delta}{\partial \theta_{\Delta,\text{i}}} \Big|_{\theta_{\Delta,\text{i}}=0°} \qquad (32)$$

If the implemented model matches the real system perfectly, the error angle disappears if no current angle deviation is present, which yields:

$$\theta_\Delta \Big|_{\theta_{\Delta,\text{i}}=0°} \approx 0° \qquad (33)$$

and (32) simplifies to:

$$\theta_\Delta \approx \theta_{\Delta,\text{i}} \cdot \frac{\partial \theta_\Delta}{\partial \theta_{\Delta,\text{i}}} \Big|_{\theta_{\Delta,\text{i}}=0°} \qquad (34)$$

It can be assumed, that the current angle deviation $\theta_{\Delta,\text{i}}$ is generally caused by an initial estimation error of the rotor angle $\theta_{\Delta,\text{init}}$. If it is further assumed that the initial rotor angle estimation error directly influences the current angle (in reality the voltage vector is rotated directly and the current vector angle consequently follows a transient process). It follows:

$$-\theta_{\Delta,\text{i}} \approx \theta_{\Delta,\text{init}} \qquad (35)$$

It is evident, that the initial estimation error must not cause an increased angle error. Thus, the following convergence criterion can be deduced from (34):

$$\Gamma = -\frac{\partial \theta_\Delta}{\partial \theta_{\Delta,\text{i}}} \Big|_{\theta_{\Delta,\text{i}}=0°} < 1 \quad \forall \, \boldsymbol{i}_\text{s}^\text{r}, \theta_\text{el} \qquad (36)$$

If the criterion is met, the rotor angle error reduces after a current angle deviation. It should be mentioned that the criterion guarantees the convergence of the encoderless model, but not the stability of the entire drive system, which must be assessed separately. Nevertheless, the convergence of the encoderless algorithm is essential for the stability of the entire drive system. The criterion can be assessed with a reasonable amount of effort, either by measurements or by means of an FEM-based simulation procedure as shown in the following sections. However, it also underlies two limitations:

- The derivation of the criterion implies that all model parameters are dependent on the currents only. This can be assumed to be true for machines with distributed windings, as the RSM is. However, the parameters of machines with concentrated windings and strong harmonic anisotropies are rotor angle dependent also. There might be a limitation for such types of machine, therefore.
- The derivation of the criterion does not consider any filter properties. A prediction of the convergence region by FEM results could become inaccurate when applying algorithms with complex filters (e.g. Kalman filter) on the test bench. However, such complex filters are usually less applied in conjunction with injection-based methods (they are commonly applied in conjunction with EMF-based methods). Most injection-based methods rely on filtering, which is based on a PLL. The
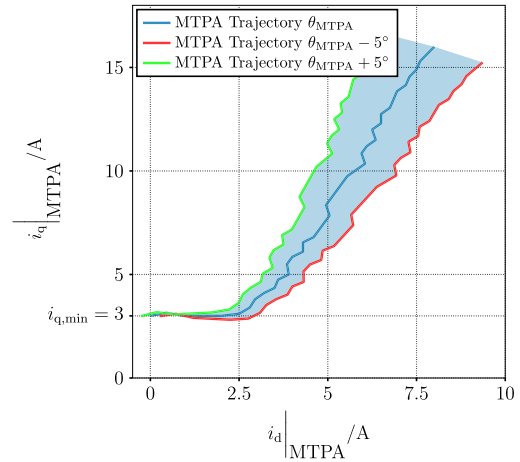

FIGURE 8. Intended MTPA trajectory and trajectories with a deviation from the current angle.

impact of the PLL filter properties is small regarding the investigated phenomenon as shown in Section VI. If the convergence criterion is measured on the test bench, all the filter properties are considered automatically and the limitation regarding observers is not present.

VIII. EMPIRICAL VERIFICATION

This section includes the verification of the stability criterion by an additional measurement procedure. The verification of the criterion is performed around the MTPA trajectory only, and not for each possible current pair i_d and i_q. Otherwise, a three-dimensional dependency would have to be assessed if the rotor angle is considered as well. By doing so, stability around the targeted MTPA curve should be guaranteed. The investigated area is illustrated by the shaded area of Fig. 8, which shows the targeted real trajectory (blue) and the trajectories with a five-degree deviation (green/red). The stability factor Γ is measured as follows. At first, the machine is operated directly on the targeted current trajectory (blue MTPA) with the current angle θ_MTPA and then on a trajectory with $\theta_\text{MTPA} - 5°$ (red MTPA) while the machine is rotated by the load machine with $n_\text{el} = 100$ rpm. Therefore all possible rotor angles are covered. This procedure is conducted in open-loop mode using the encoder. The estimation error θ_Δ is recorded throughout. The parameters of the encoderless methods are only stored along the intended MTPA trajectory at θ_MTPA (blue curve in Fig. 8). According to (31), the current angle deviation is $\theta_{\Delta,\text{i}} = -5°$ when operating along the red MTPA curve. The stability factor can then be determined using the discretized form of the criterion:

$$\Gamma = -\frac{\theta_\Delta \left(\theta_{\Delta,\text{i}} = 0°\right) - \theta_\Delta \left(\theta_{\Delta,\text{i}} = -5°\right)}{5°}$$
$$\forall \, \theta_\text{el}, \boldsymbol{i}_\text{s}^\text{r} \in \text{MTPA} \qquad (37)$$

This process is repeated for different current amplitudes for each algorithm. The results of this measurement procedure are illustrated by the contour plots. It should be noted that the

criterion could also be measured in an alternative manner by operating the machine two times along the intended trajectory using an encoder. In this case, the measurements need to be performed once at the correct current angle and once with a rotated current angle used to determine the parameters.

To verify the measurement results of the stability factor, a second measurement procedure is performed. The rotor of the machine is locked in different positions and the reference torque (MTPA) is increased up to the point $|\theta_\Delta| > 25°$. This test is conducted under closed-loop control. The maximum achieved current amplitude $|i_s^s|_{max}$ is recorded for each measurement i. This procedure is repeated four times for each rotor position to ensure reproducibility. From these four measurements the mean maximum current amplitude is calculated as follows:

$$|\overline{i_s^s}|_{max} = \frac{\sum_{i=1}^{4} |i_s^s|_{max,i}}{4} \quad (38)$$

and the sample standard deviation is determined by:

$$s = \sqrt{\frac{\sum_{i=1}^{4} \left(|i_s^s|_{max,i} - |\overline{i_s^s}|_{max}\right)^2}{4-1}} \quad (39)$$

Both measurement procedures are visualized together in one single diagram in order to verify the prediction of the criterion. The results of the locked-rotor-test are indicated by the green dots and rectangles in the diagram. The error bars indicate the sample standard deviation of the locked-rotor-test and the contour plots show the measurement results of the stability criteria according to (37).

A. MODEL IN STATOR COORDINATES

The result of the model in stator coordinates is shown in Fig. 9. The stability factor stays nearly constant for all investigated operating points. The maximum value of the stability factor is 0.12 – therefore still far from the limit. The stability criterion predicts the stable operation of the method at all investigated operating points, which is confirmed by the locked rotor test.

B. ALTERNATING INJECTION

The results of the Alternating Injection are shown in Fig. 10. The stability factor deteriorates with increased current amplitude, which confirms the well-known experience of a reduced performance in deep magnetic saturation. The stability criterion predicts the points of instability very well around 17A. The measurements are highly reproducible, which is shown by the low standard deviation. The sinusoidal fluctuation (sixth harmonic) of the stability factor is caused by the winding arrangement of the machine. The results of the new stability criterion and the stability criterion of [16] are compared. The criterion of [16] is shown in Fig. 11. The Factor k must be greater than zero according to the authors of [16]. Both predictions are similar. This was expected
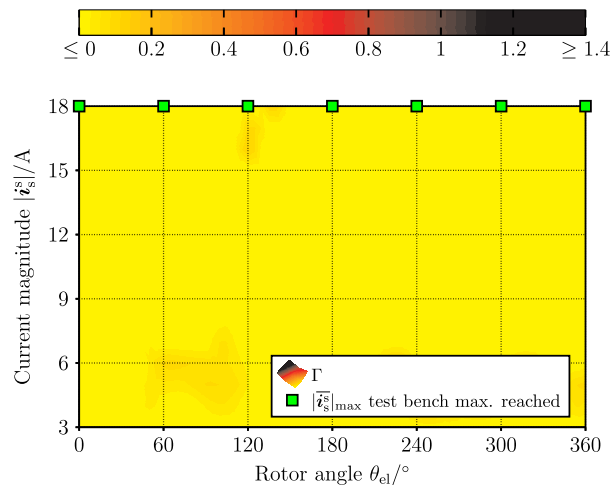
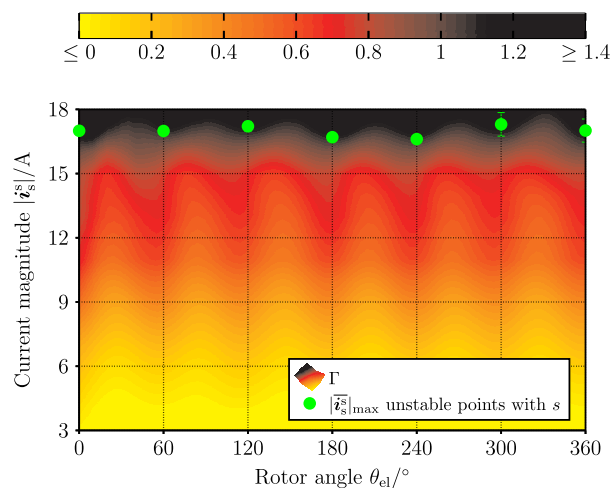FIGURE 9. Measurement results of the model in stator coordinates.

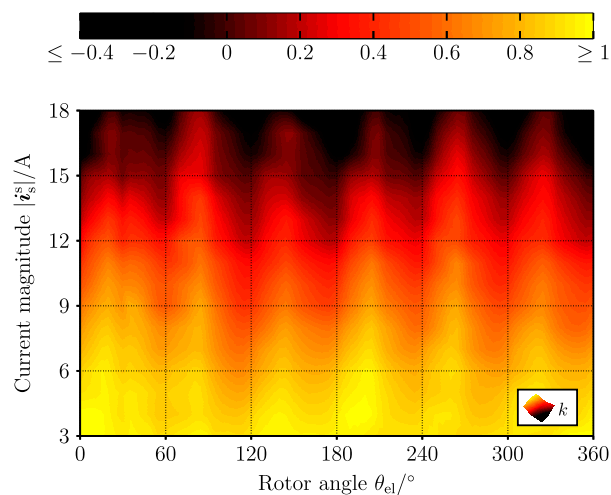FIGURE 10. Measurement results of the Alternating Injection model.

FIGURE 11. Measured stability factor $k \overset{!}{>} 0$ according to [16, p. 9].

because the criterion of [16] analyses exactly the structure of the Alternating Injection model.
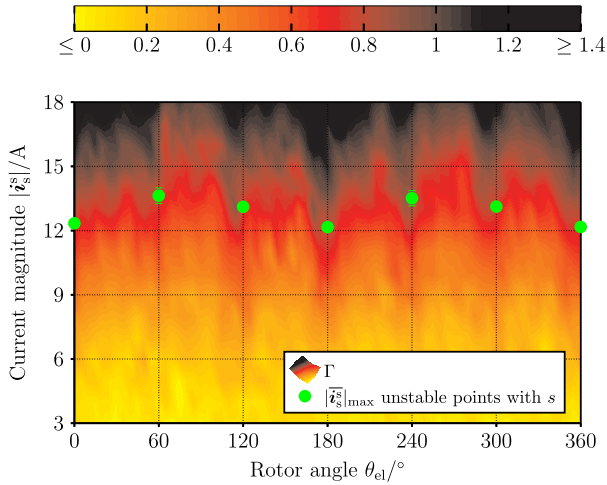
FIGURE 12. Measurement results of the Arbitrary Injection model with online $\acute{Y}_\Sigma$ estimation.

FIGURE 13. Measurement results of the Arbitrary Injection with LUT-based $\acute{Y}_\Sigma$ estimation.

C. ARBITRARY INJECTION WITH ONLINE $\acute{Y}_\Sigma$ ESTIMATION

The results of the Arbitrary Injection model with online $\acute{Y}_\Sigma$ estimation are shown in Fig. 12. The stability factor deteriorates with increased current amplitude, which corresponds to the well-known experience of reduced performance in deep magnetic saturation. The stability criterion predicts the points of instability very well around 13A and it also predicts the periodic fluctuation. The measurements are highly reproducible, as evidenced by the low standard deviation. The fluctuation of the stability factor and the unstable points might be caused by a deviation of $\acute{Y}_\Sigma$, which leads to an angle error oscillating with twice the electrical angle. This effect is superimposed by the effect caused by the winding arrangement (sixth harmonic).

D. ARBITRARY INJECTION WITH LUT-BASED $\acute{Y}_\Sigma$ ESTIMATION

The results of the Arbitrary Injection with LUT-based $\acute{Y}_\Sigma$ estimation are depicted in Fig. 13. The stability factor deteriorates with increasing current amplitude and shows a strong oscillation with twice the electrical angle. The criterion predicts the points of instability very well. The measurements are again, highly reproducible. The periodic fluctuation of the stability factor is caused by a deviation of $\acute{Y}_\Sigma$, which can be explained as follows. A deviation between the estimated and actual operating point becomes more significant if $\acute{Y}_\Sigma$ is stored in an LUT because it is now dependent on the estimated operating point (different to the case from the online estimation). In this case, the error angle θ_Δ has a strong dependency on the mean admittance $\acute{Y}_\Sigma$ (it causes a second harmonic in the angle error), which again is dependent on the current angle deviation $\theta_{\Delta,i}$. However, this effect causes not only a reduction (along the rotor angle) in the maximum current amplitude but also an increase in the achievable current amplitude can occur if the constellation is beneficial.
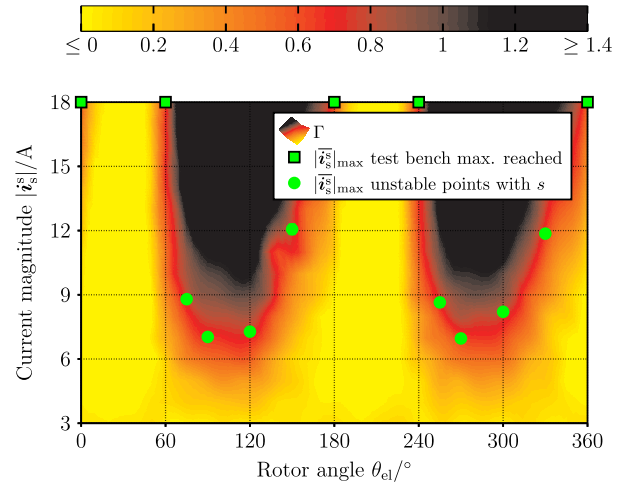
E. EEMF

The results of the EEMF are shown in Fig. 14. The stability factor deteriorates with increased current amplitude for all rotor angles. The general tendency of the stability criterion fits the points of instability. However, the prediction is not very accurate. This can be explained as follows. On one hand, the assumption made in equation (33) is not fulfilled and the scheme shows strong estimation errors on the targeted current trajectory. This again can be explained by equation (28). (28) infers that parts of the estimation equation disappear at a standstill, resulting in a lower estimation quality. Compared to the results of Fig. 7 (magenta), where the estimation performance was okay, the machine is at a standstill for the green dots. However, the measurements of the stability factor are performed at $n_{el} = 100$ rpm. Due to the differences in rotational speed, different results are to be expected. Contrary to the other methods, the stability factor also depends on the speed $\Gamma = f\left(i_s^r, \theta_{el}, \omega_{el}\right)$. Thus, the model cannot be considered to be mainly dependent on the current angle operating point as it was assumed when deriving the convergence criterion. The reason why the locked rotor test results are above the prediction of the criterion remains to be investigated further.

From all the measurements of this section (Fig. 9-14), it can be concluded, that the new stability criterion is able to predict the overload limitation of most of the models. It has been proven for the first time that parameter uncertainties due to the deviation between the estimated and actual operating point are the cause of the issue in deep magnetic saturation. The machine itself has only a small impact on this issue. However, up until now this could only be considered true for the RSM and remains to be verified for other types of synchronous machines. By comparing the measurements taken in Section VI with the results of this section, it can be seen that some of the schemes reach slightly higher current amplitudes when the machine is rotating. This can be explained by assuming that the machine overruns the unstable regions when it is rotating. This behavior might be dependent on the
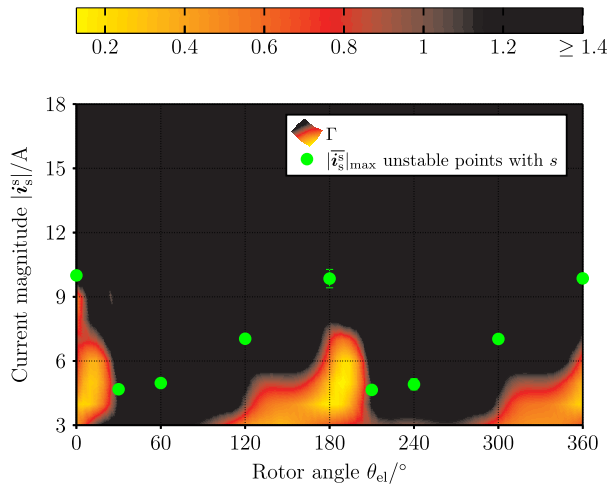
FIGURE 14. Measurement results of the EEMF-based model.

relationship between the PLL settings and the actual electrical speed as well as on the ratio of stable to unstable regions over the entire range of 360°. However, analysis regarding this effect does not form part of this work.

IX. PREDICTION OF THE CONVERGENCE REGION USING FEM SIMULATION RESULTS

FEM simulations are the standard tool for the design of electrical machines and might be useful to predict the convergence region by means of the proposed convergence criterion. The prediction of the convergence region at an early design stage of the machine has a big practical relevance, since it could be used to verify whether the desired torque can be reached by the intended combination of machine and encoderless algorithm. Modifications to the algorithm or the machine can then be done without building a prototype first.

The following section shows how to predict the convergence region using FEM simulation results. The workflow is briefly discussed and the simulation results are compared with the results of the locked rotor test from the real test bench, which were described in Section VIII. The FEM simulation was performed using the tool ©Ansys Maxwell.

Several simulation steps are necessary to derive the desired inductance parameters used by the models with their dependencies on the currents, the rotor position, and also on the current angle deviation as it is required for the convergence criterion. The same procedure, as it is proposed in [22], can be used to derive the required inductance parameters. Since the procedure is detailedly discussed in [22], only the main two steps of the simulation procedure are briefly summarized in the following:

- The first simulation step is conducted to determine the flux linkage maps of the machine in dependency on the currents of the rotor fixed reference frame. After that, the MTPA trajectory is determined from the simulated flux linkage maps. The subsequent simulations are then regarding the MTPA trajectory only to reduce

the simulation effort in the following simulation step. This simplification is valid, since most injection-based methods are used along the MTPA curve.

- The second simulation step is carried out to derive the electrical parameters of the machine. The parameters must be determined in dependency on the following independent variables, the rotor position θ_{el}, the current amplitude of the currents, which are referred to the MTPA trajectory $\left|i^r_{s,MTPA}\right|$, and on the current angle deviation $\theta_{\Delta,i}$. Thus, the simulation must be performed for different combinations of θ_{el} and $\left|i^r_{s,MTPA}\right|$ for at least two values of $\theta_{\Delta,i}$ to be able to determine the partial derivative of the convergence criterion (36).

The FEM simulations are used to determine the electrical parameters of the machine with the desired dependencies. However, this is not enough to consider the specificities in the structure of each of the injection-based encoderless algorithms. These specificities must be considered in the third and final calculation process, where the structure of each of the algorithms is considered by a specific estimation equation. This specific estimation equation is intended to emulate the structure of the specific algorithm and how it estimates the rotor position, therefore. The specific estimation equations are kept as simple as possible in the following, without considering filter properties. Ultimately, the equation must emulate the feedback paths due to estimated parameters, as they are shown in blue in Fig. 1-4, since this feedback paths are the main difference between the algorithms.

The simulative prediction is done for three of the algorithms only, the Alternating Injection (IV-A), the Arbitrary Injection with online estimation of the isotropic part, and for the Arbitrary Injection with LUT-based estimation of the isotropic part (both described in IV-B). The model in stator coordinates (IV-C) is not verified, since it has no feedback of estimated quantities in its structure, which could be considered in the specific estimation equation. Thus, the convergence criterion would be zero (zero in the numerator) in any operating point for the model in stator coordinates. The EEMF based model (IV-D) was also not verified by the simulation process, since a further dependency must be considered in the FEM simulation (the speed ω_{el}) to consider all of the feedback, as was discussed in Subsection VIII-E. This speed dependency is not covered by the convergence criterion anyway, that is the reason why the criterion was not predicted simulatively for the EEMF.

The specific estimation equations used for the prediction are briefly discussed in the following for each of the three models investigated. The electrical parameters were determined by the FEM simulation process as described above and in [22]. A current angle deviation of $\theta_{\Delta,i} = -8°$ was used in the FEM simulation process to record the dependency on the current angle deviation.

The predicted convergence criteria are shown and compared with the results of the locked rotor test, which are indicated by the green dots and rectangles.
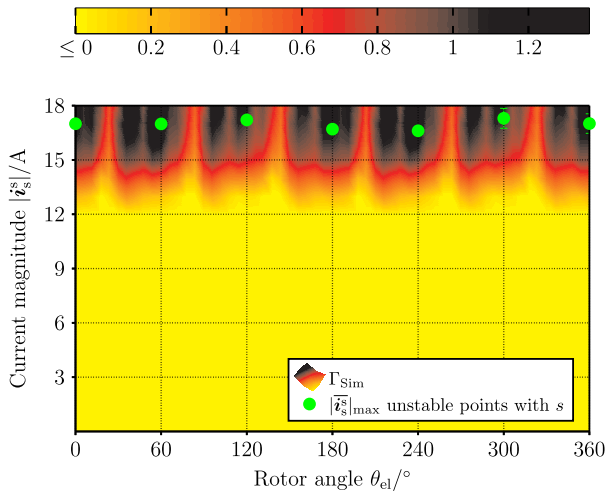
FIGURE 15. Predicted convergence criterion using FEM simulation results for the Alternating Injection model.

A. ALTERNATING INJECTION

The structure of the Alternating Injection, as shown in Fig. 1, reveals that estimated parameters are used in the rotor position assignment algorithm only. Therefore, it can be assumed that this algorithm always converges to the correct anisotropy angle θ_A. This means that a rotor position estimation error θ_Δ (due to a current angle deviation $\theta_{\Delta,i}$) can only be caused by the rotor position assignment algorithm. Thus, the entire estimation error occurs due to the wrong parameters used to determine the misalignment angle θ_δ as defined in equation (11) and used in the rotor position assignment algorithm. The convergence criterion can therefore be estimated as follows for the Alternating Injection using the FEM derived inductance parameters (more details in Appendix X-A):

$$\Gamma_{\text{Sim}} = -\frac{\Delta\theta_{\Delta,\text{Alt.}}}{8°} \quad \forall\, \theta_{\text{el}}, \boldsymbol{i}_s^r \in \text{MTPA} \tag{40}$$

with the following definition of the numerator:

$$\Delta\theta_{\Delta,\text{Alt.}} = \frac{1}{2}\arctan\left(\frac{\acute{L}_{\text{dq}}\left(\theta_{\Delta,i} = 0°\right)}{\acute{L}_\Delta\left(\theta_{\Delta,i} = 0°\right)}\right) \dots$$
$$\dots - \frac{1}{2}\arctan\left(\frac{\acute{L}_{\text{dq}}\left(\theta_{\Delta,i} = -8°\right)}{\acute{L}_\Delta\left(\theta_{\Delta,i} = -8°\right)}\right)$$
$$\forall\, \theta_{\text{el}}, \boldsymbol{i}_s^r \in \text{MTPA} \tag{41}$$

The result is shown in Fig. 15. Since the prediction of the simulation is near to the results of the locked rotor test and similar to the measured convergence criterion, which is shown in Fig. 10, the simulation process conducted is assumed to be correct. The small differences between the simulated and measured criteria might be caused by a difference between the actual saturation curve of the iron and the underlying saturation curve used in the FEM simulation. The simulated machine seems to saturate earlier than the real one.

B. ARBITRARY INJECTION WITH ONLINE $\acute{Y}_\Sigma$ ESTIMATION

The structure of the Arbitrary Injection with online estimation of the isotropic part, as shown in Fig. 2, suggests that estimated parameters are used in the rotor position assignment algorithm only. In Fig. 2 it is assumed that the anisotropy angle is always estimated correctly due to a perfect online estimation of the isotropic part. However, this cannot be expected to be true in reality due to estimation errors of the mean admittance. Therefore, the rotor position estimation error θ_Δ occurs not only due to the wrong parameters in the rotor position assignment algorithm but also due to a slight deviation of the isotropic part $\acute{Y}_\Sigma$. This slight deviation in the isotropic part causes estimation errors in the anisotropy angle θ_A.

In the following, it is assumed that the anisotropy angle is calculated by an atan2 function, once without current angle deviation and once with $\theta_{\Delta,i} = -8°$. The specific estimation equation used in the following is based on the admittance model (13) since it forms the base for the derivation of the Arbitrary Injection (17). The shape of the voltage injection used by the Arbitrary Injection has an influence as well, as the shape of the voltage injection determines which entries of the admittance matrix (13) are "*active*" and how the current derivatives are modulated, as stated by equation (17). For simplicity, it is assumed that the voltage injection causes the following admittance vector to be "*active*" (pure alpha injection):

$$\boldsymbol{y}_s^s = \begin{bmatrix} \acute{Y}_\Sigma \\ 0 \end{bmatrix} + \acute{Y}_A \begin{bmatrix} \cos\left(2\theta_A\right) \\ \sin\left(2\theta_A\right) \end{bmatrix} \tag{42}$$

The workflow of the Arbitrary Injection is as follows (Fig. 2). The anisotropy angle is determined by subtracting the estimated mean admittance from the admittance vector first (20) and then applying the atan2 function by the result, this yields:

$$\hat{\theta}_A = \frac{1}{2}\text{atan2}\left(\frac{\acute{Y}_A\sin\left(2\theta_A\right)}{\acute{Y}_\Sigma - \hat{\acute{Y}}_\Sigma + \acute{Y}_A\cos\left(2\theta_A\right)}\right) \tag{43}$$

Equation (43) shows that a wrongly estimated mean admittance $\hat{\acute{Y}}_\Sigma$ must cause an estimation error of the anisotropy angle.

The estimated mean admittance was set to $\hat{\acute{Y}}_\Sigma = 1.05 \cdot \acute{Y}_\Sigma$ to simulate a slight deviation in the estimation of the mean admittance. This +5% deviation was considered to be present with and without current angle deviation, resulting in the following equation for the estimation of the anisotropy angle by substitution in (43).

$$\hat{\theta}_{A,\text{Sim.}}\left(\theta_{\Delta,i}\right)$$
$$= \frac{1}{2}\text{atan2}\left(\frac{\acute{Y}_A\left(\theta_{\Delta,i}\right)\sin\left(2\theta_A\left(\theta_{\Delta,i}\right)\right)}{-0.05\acute{Y}_\Sigma\left(\theta_{\Delta,i}\right) + \acute{Y}_A\left(\theta_{\Delta,i}\right)\cos\left(2\theta_A\left(\theta_{\Delta,i}\right)\right)}\right) \tag{44}$$

All the inductance parameters as well as the anisotropy angle must be considered to be current angle deviation dependent.

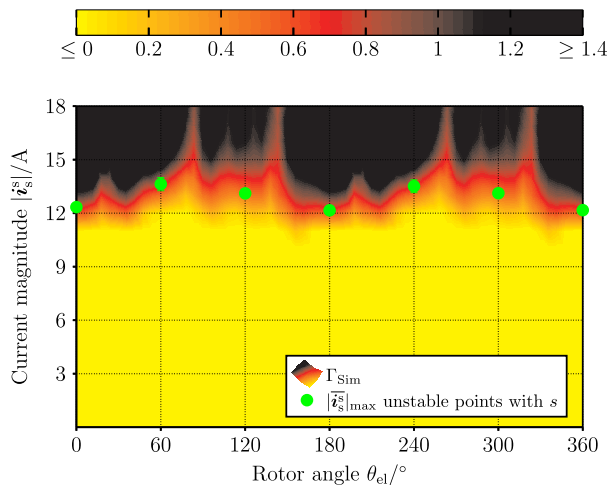**FIGURE 16.** Predicted convergence criterion using FEM simulation results for the Arbitrary Injection model with online $\acute{Y}_\Sigma$ estimation.
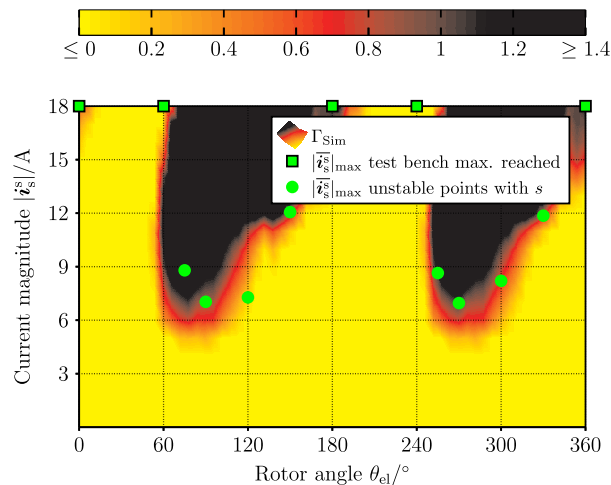

FIGURE 17. Predicted convergence criterion using FEM simulation results for the Arbitrary Injection with LUT-based $\acute{Y}_\Sigma$ estimation.

Equation (44) can then be used to estimate the convergence criterion as follows (more details in Appendix X-B):

$$\Gamma_{\text{Sim}} = -\frac{\Delta\theta_{\Delta,\text{Arb.}}}{8°} \quad \forall\, \theta_{\text{el}}, \boldsymbol{i}_s^r \in \text{MTPA} \tag{45}$$

with the following definition of the numerator:

$$\Delta\theta_{\Delta,\text{Arb.}} = \hat{\theta}_{A,\text{Sim.}}\left(\theta_{\Delta,i} = 0°\right) - \hat{\theta}_{A,\text{Sim.}}\left(\theta_{\Delta,i} = -8°\right) \tag{46}$$

The derivation conducted in Appendix X-B shows that the estimated misalignment angle has no impact on the convergence criterion, if it is stored according to the current amplitude only ($\hat{\theta}_\delta = f(\left|\boldsymbol{i}_{s,\text{MTPA}}^s\right|)$). The convergence criterion shown in Fig. 16 shows a good agreement with the results of the locked rotor test and the measured criterion shown in Fig. 12, this property and the simulation procedure can be assumed to be true, therefore. The simulation results also depict the same weak second harmonic in the convergence region as the locked rotor test. Nevertheless, the simulated criterion seems to be more strict compared to the measured convergence criterion of Fig. 12. This might be caused by a difference between the actual saturation curve of the iron and the one used in the FEM simulation. The simulated machine seems to saturate earlier than the real one, the same tendency can be observed for the results of the Alternating Injection.

C. ARBITRARY INJECTION WITH LUT-BASED $\acute{Y}_\Sigma$ ESTIMATION

The measurement results of the convergence criterion have already depicted big differences between the two implementation versions of the Arbitrary Injection. The difference is caused by the implementation of the mean admittance, which is stored (in the following case) for a fixed current trajectory (MTPA) when an LUT is used and does not follow any deviations due to a current angle deviation $\theta_{\Delta,i}$. The estimated mean admittance can therefore be understood as

$\hat{\acute{Y}}_\Sigma = \acute{Y}_\Sigma\left(\theta_{\Delta,i} = 0°\right)$, independent of the actual current angle deviation. The rest of the model remains the same as for the Arbitrary Injection with online estimation. Equation (43) can therefore be adapted to this property of the mean admittance, resulting in the following equation for the estimation of the anisotropy angle:

$$\hat{\theta}_{A,\text{Sim.}}\left(\theta_{\Delta,i}\right)$$
$$= \frac{1}{2}\text{atan2}\Big(\acute{Y}_A\left(\theta_{\Delta,i}\right)\sin\left(2\theta_A\left(\theta_{\Delta,i}\right)\right)/\ldots$$
$$\ldots\left(\acute{Y}_\Sigma\left(\theta_{\Delta,i}\right) - \hat{\acute{Y}}_\Sigma + \acute{Y}_A\left(\theta_{\Delta,i}\right)\cos\left(2\theta_A\left(\theta_{\Delta,i}\right)\right)\right)\Big) \tag{47}$$

with

$$\hat{\acute{Y}}_\Sigma = \acute{Y}_\Sigma\left(\theta_{\Delta,i} = 0°\right)\Big|_{\text{MTPA}} \tag{48}$$

Equation (47) is then inserted in (46) and then in (45) to derive the convergence criterion for Arbitrary Injection with LUT-based estimation of the isotropic part, resulting in the estimated convergence criterion shown in Fig. 17. The simulation is in good agreement with the results of the locked rotor test. It follows the strong variations with twice the electrical speed very well. The simulated one seems to be more strict compared to the measured convergence criterion shown in Fig. 13, which is probably caused by a difference between the underlying magnetic saturation curve and the real one.

D. INTERPRETATION OF THE SIMULATION RESULTS

The results of the proposed simulation procedure show good agreement with the results of the test bench. This allows the maximum achievable torque to be estimated at an early design stage of the machine, without the need of testing it on a prototype. Improvements to the system can be considered as early as during the FEM process.

The difficulty in the simulation procedure is finding a proper estimation equation, which can emulate the structure of the specific algorithm. However, the FEM procedure used to determine the parameters is simple and straightforward.

The proposed procedure can be used to get a fast prediction of the convergence criteria once the FEM results are available. Simple post-processing, e.g. in a ©MATLAB m-file, can be used to calculate the convergence criterion.

An extended simulation procedure could be conducted using the FEM results in a detailed simulation model (e.g. ©MATLAB Simulink), including the entire control structure. The filter properties (also of observer-based estimators) of the system would be considered in this case. However, such a procedure would be very time-consuming and is therefore not proposed in this work. The proposed simulation procedure was able to predict the behavior on the test bench very well even without considering filter effects.

X. CONCLUSION

This work has analyzed the impact of different injection-based encoderless control algorithms on the overload capability problem. The investigations were based on an RSM. A comparative investigation (Section VI) of different algorithms, regarding their maximum achievable current amplitude, was performed. Such a comparative investigation had not been performed thus far. This basic investigation has already uncovered significant differences between the algorithms. Based on the new findings, a novel stability criterion for the RSM has been derived. The new stability criterion can predict the overload limit of several algorithms by assessing the impact of an operating point deviation between the actual and the estimated operating point. The prediction for several algorithms was not possible based on already existing criteria, because they were based on a specific model.

Based on the new criterion and its good prediction for several algorithms it is generally confirmed, that incorrect estimated parameters are the cause of the overload capability problem. The incorrect parameters are caused by the difference between the actual and estimated operating point of the machine. This behavior is reasonable and can only be avoided by making the parameters independent of an operating point deviation. This conclusion is confirmed by the results of the model in stator coordinates, which always knows the actual parameters.

Finally, an FEM-based simulation procedure was proposed, which can precisely predict the convergence region for different injection-based encoderless algorithms.

The general conclusion can be made that the more estimated parameters are used, the worse the behavior in deep saturation. It is also shown that stable operation is mainly a property of the algorithm used and less of the design of the RSM. An optimization of the machine is therefore only meaningful, if the specificities of the algorithm are considered

in the optimization process. The work also demonstrated that even small differences in the implementation, e.g. an LUT stored mean admittance, can have a big impact on the overload capability. This should be considered when the algorithms are implemented.

The following enumeration is intended to briefly summarize the most important contributions of this work and to answer the open subjects stated in the introduction part:

- A new convergence criterion was derived. It reliably predicts the convergence region for several injection-based models, which was not possible with existing criteria.
- An investigation of the overload capability of several injection-based models was conducted, which had not been done in the research literature before. Significant differences between the models could be revealed.
- It has been shown that the prediction of the convergence region is also possible by means of FEM simulation results, opening new possibilities in the practical application. The achievable current amplitude (torque) can already be predicted at an early design stage of the machine. It can be assessed whether the required torque can be reached with the intended combination of machine and encoderless algorithm. Thus, the machine or the algorithm can be modified early in the development process, without building a prototype of the system first. However, the optimization must be carried out considering the specificities of the algorithm.
- The new convergence criterion assesses the dependency of the estimation error on an incorrect current angle, which is used to determine the specific model parameters. Since the predictions are in harmony with the measurement results, the assumptions made during the derivation of the criterion can be taken as true. As a consequence of the correct assumptions, the parameters stored according to an unknown reference system (when operating encoderlessly, e.g. d-q-system) are the cause of the overload capability problem.

In further works, the idea of the operating point deviation could be extended to include the rotor angle dependency of the inductances as well (not just the current angle). It might be possible to find a convergence criterion for machines with strong harmonic anisotropies using such an extension. Furthermore, the proposed criterion was verified on the most popular injection-based models but could be verified for further models and also be extended to different types of observers in the future.

APPENDIX

The appendix includes the derivations of the simulated convergence criteria in a compact form. Please note the difference between estimated and real parameters, which is important for the derivation. The expressions inside the brackets are shortened for a compact illustration, e.g. $\theta_\Delta \left(0°\right) \widehat{=} \theta_\Delta \left(\theta_{\Delta,\mathrm{i}} = 0°\right)$.

A. SUB-CALCULATION FOR THE SIMULATIVE PREDICTION OF THE ALTERNATING INJECTION

The discrete version of the convergence criterion, as it is depicted in (37), forms the base:

$$\Gamma_{Sim} = -\frac{\Delta\theta_{\Delta}}{\Delta\theta_{\Delta,i}} = -\frac{\theta_{\Delta}(0°) - \theta_{\Delta}(-8°)}{0° - -8°}$$

$$= -\frac{\hat{\theta}_{el}(0°) - \theta_{el} - \hat{\theta}_{el}(-8°) + \theta_{el}}{8°}$$

The rotor position assignment algorithm is implemented in a way that the misalignment angle is always estimated along the intended MTPA trajectory ($\hat{\theta}_{\delta}(0°)$). This results in the following criterion which relies on the actual (not the estimated) misalignment angle θ_{δ}:

$$\Gamma_{Sim} = -\frac{\theta_{A}(0°) - \hat{\theta}_{\delta}(0°) - \theta_{A}(-8°) + \hat{\theta}_{\delta}(0°)}{8°}$$

$$= -\frac{\theta_{A}(0°) - \theta_{A}(-8°)}{8°}$$

$$= -\frac{\theta_{el} + \theta_{\delta}(0°) - \theta_{el} - \theta_{\delta}(-8°)}{8°}$$

$$= -\frac{\theta_{\delta}(0°) - \theta_{\delta}(-8°)}{8°}$$

$$= -\frac{\Delta\theta_{\Delta,Alt.}}{8°}$$

B. SUB-CALCULATION FOR THE SIMULATIVE PREDICTION OF THE ARBITRARY INJECTION

The discrete version of the convergence criterion, as it is depicted in (37), forms the base:

$$\Gamma_{Sim} = -\frac{\Delta\theta_{\Delta}}{\Delta\theta_{\Delta,i}} = -\frac{\theta_{\Delta}(0°) - \theta_{\Delta}(-8°)}{0° - -8°}$$

$$= -\frac{\hat{\theta}_{el}(0°) - \theta_{el} - \hat{\theta}_{el}(-8°) + \theta_{el}}{8°}$$

The rotor position assignment algorithm is implemented in a way that the misalignment angle is always estimated along the intended MTPA trajectory ($\hat{\theta}_{\delta}(0°)$). The anisotropy angle is an estimated quantity for this algorithm, other than for the Alternating Injection.

$$\Gamma_{Sim} = -\frac{\hat{\theta}_{A}(0°) - \hat{\theta}_{\delta}(0°) - \hat{\theta}_{A}(-8°) + \hat{\theta}_{\delta}(0°)}{8°}$$

$$= -\frac{\hat{\theta}_{A}(0°) - \hat{\theta}_{A}(-8°)}{8°}$$

with the definition of the specific estimation equation of the anisotropy angle (either (44) or (47)) follows:

$$= -\frac{\hat{\theta}_{A,Sim.}(0°) - \hat{\theta}_{A,Sim.}(-8°)}{8°}$$

REFERENCES

[1] K. Iizuka, H. Uzuhashi, M. Kano, T. Endo, and K. Mohri, "Microcomputer control for sensorless brushless motor," *IEEE Trans. Ind. Appl.*, vol. IA-21, no. 3, pp. 595–601, May 1985, doi: 10.1109/TIA.1985.349715.

[2] S. Bolognani, R. Oboe, and M. Zigliotto, "Sensorless full-digital PMSM drive with EKF estimation of speed and rotor position," *IEEE Trans. Ind. Electron.*, vol. 46, no. 1, pp. 184–191, Feb. 1999, doi: 10.1109/41.744410.

[3] P. L. Jansen and R. D. Lorenz, "Transducerless position and velocity estimation in induction and salient AC machines," *IEEE Trans. Ind. Appl.*, vol. 31, no. 2, pp. 240–247, Mar. 1995, doi: 10.1109/28.370269.

[4] M. J. Corley and R. D. Lorenz, "Rotor position and velocity estimation for a salient-pole permanent magnet synchronous machine at standstill and high speeds," *IEEE Trans. Ind. Appl.*, vol. 34, no. 4, pp. 784–789, Jul. 1998, doi: 10.1109/28.703973.

[5] P. Landsmann, D. Paulus, and R. Kennel, "Silent and parameter independent hybrid sensorless control for SPMSM based on current oversampling," in *Proc. IEEE Int. Symp. Sensorless Control Electr. Drives Predictive Control Electr. Drives Power Electron. (SLED/PRECEDE)*, Oct. 2013, pp. 1–8, doi: 10.1109/SLED-PRECEDE.2013.6684513.

[6] R. Leidhold and P. Mutschler, "Injection of a carrier with higher than the PWM frequency for sensorless position detection in PM synchronous motors," in *Proc. 13th Int. Power Electron. Motion Control Conf.*, Sep. 2008, pp. 1353–1358, doi: 10.1109/EPEPEMC.2008.4635456.

[7] P. Landsmann, "Sensorless control of synchronous machines by linear approximation of oversampled current," Ph.D. dissertation, Dept. Elect. Eng. Inf. Technol., Tech. Univ. Munich, Munich, Germany, 2014.

[8] P. Landsmann, D. Paulus, P. Stolze, and R. Kennel, "Saliency based encoderless predictive torque control without signal injection for a reluctance synchronous machine," in *Proc. 14th Int. Power Electron. Motion Control Conf.*, Sep. 2010, pp. 1–10, doi: 10.1109/EPEPEMC.2010.5606557.

[9] M. W. Degner and R. D. Lorenz, "Using multiple saliencies for the estimation of flux, position, and velocity in AC machines," *IEEE Trans. Ind. Appl.*, vol. 34, no. 5, pp. 1097–1104, Sep. 1998, doi: 10.1109/28.720450.

[10] D. Paulus, P. Landsmann, S. Kuehl, and R. Kennel, "Arbitrary injection for permanent magnet synchronous machines with multiple saliencies," in *Proc. IEEE Energy Convers. Congr. Expo.*, Denver, CO, USA, May 2013, pp. 511–517, doi: 10.1109/ECCE.2013.6646744.

[11] P. Vaclavek, P. Blaha, and I. Herman, "AC drive observability analysis," *IEEE Trans. Ind. Electron.*, vol. 60, no. 8, pp. 3047–3059, Aug. 2013, doi: 10.1109/TIE.2012.2203775.

[12] N. Bianchi and S. Bolognani, "Influence of rotor geometry of an IPM motor on sensorless control feasibility," *IEEE Trans. Ind. Appl.*, vol. 43, no. 1, pp. 87–96, Jan./Feb. 2007, doi: 10.1109/TIA.2006.887317.

[13] N. Bianchi, E. Fornasiero, and S. Bolognani, "Effect of stator and rotor saturation on sensorless rotor position detection," *IEEE Trans. Ind. Appl.*, vol. 49, no. 3, pp. 1333–1342, May 2013, doi: 10.1109/TIA.2013.2253437.

[14] A. K. Jebai, "Sensorless control of synchronous permanent magnet motors by signal injection," Ph.D. dissertation, Dept. Math. Control, Ecole Nat. Suprieure des mines de Paris, Paris, France, 2013.

[15] R. Kowalski and J. Windelberg, "Anisotropy identification for electromechanical flight actuators with sensorless rotor angle detection," *IEEE Trans. Transport. Electrific.*, vol. 6, no. 4, pp. 1448–1456, Dec. 2020, doi: 10.1109/TTE.2020.3008302.

[16] W. Hammel, P. Landsmann, and R. M. Kennel, "Operating point dependent anisotropies and assessment for position-sensorless control," in *Proc. 18th Eur. Conf. Power Electron. Appl.*, Karlsruhe, Germany, Sep. 2016, pp. 1–10, doi: 10.1109/EPE.2016.7695509.

[17] M. Roetzer, U. Vollmer, and R. Kennel, "Anisotropy-based position estimation for highly-saturated permanent magnet synchronous machines in slowly-sampled control systems," in *Proc. 19th Eur. Conf. Power Electron. Appl.*, Sep. 2017, p. 10, doi: 10.23919/EPE17ECCEurope.2017.8099092.

[18] Y. Kwon, J. Lee, and S. Sul, "Full torque-range low-speed sensorless drive for heavily saturated IPMSMs by manipulation of convergence point," in *Proc. IEEE Energy Convers. Congr. Expo. (ECCE)*, Oct. 2017, pp. 865–872, doi: 10.1109/ECCE.2017.8095876.

[19] Y. Kwon, J. Lee, and S. Sul, "Extending operational limit of IPMSM in signal-injection sensorless control by manipulation of convergence point," *IEEE Trans. Ind. Appl.*, vol. 55, no. 2, pp. 1574–1586, Mar./Apr. 2019, doi: 10.1109/TIA.2018.2882483.

[20] K. Kang Huh and D. Pan, "System and method for sensorless control of electric machines using magnetic alignment," U.S. Patent 009 948 224 B1, Apr. 17, 2018.

[21] V. Manzolini and S. Bolognani, "On the rotor position self-sensing capability of reluctance and IPM synchronous motors," *IEEE Trans. Ind. Appl.*, vol. 56, no. 4, pp. 3755–3766, Jul./Aug. 2020, doi: 10.1109/TIA.2020.2984406.

[22] M. Laumann, M. J. Kamper, C. Weiner, and R. Kennel, "FEM based analysis of the impact of temperature on the stability range of anisotropy based encoderless control schemes," in *Proc. IEEE Int. Conf. Ind. Technol. (ICIT)*, Melbourne, VIC, Australia, Feb. 2019, pp. 261–266, doi: 10.1109/ICIT.2019.8754910.

[23] M. Berto, L. Alberti, V. Manzolini, and S. Bolognani, "Computation of self-sensing capabilities of synchronous machines for rotating high frequency voltage injection sensorless control," *IEEE Trans. Ind. Electron.*, vol. 69, no. 4, pp. 3324–3333, Apr. 2022, doi: 10.1109/TIE.2021.3071710.

[24] M. Barcaro, M. Morandin, T. Pradella, N. Bianchi, and I. Furlan, "Iron saturation impact on high-frequency sensorless control of synchronous permanent-magnet motor," *IEEE Trans. Ind. Appl.*, vol. 53, no. 6, pp. 5470–5478, Dec. 2017, doi: 10.1109/TIA.2017.2731298.

[25] L. Chen, M. Roetzer, G. Goetting, and I. Hahn, "Design of highly-saturated permanent magnet synchronous machines for torque ripple optimized self-sensing control," in *Proc. IEEE Int. Symp. Sensorless Control Electr. Drives (SLED)*, Sep. 2017, pp. 1–6, doi: 10.1109/SLED.2017.8078418.

[26] G. Bacco, S. Bolognani, N. Bianchi, and V. Manzolini, "Self-sensing-oriented optimization of synchronous reluctance machine design," in *Proc. IEEE 10th Int. Symp. Sensorless Control Electr. Drives (SLED)*, Sep. 2019, pp. 1–6, doi: 10.1109/SLED.2019.8896320.

[27] M. Linke, R. Kennel, and J. Holtz, "Sensorless position control of permanent magnet synchronous machines without limitation at zero speed," in *Proc. IEEE 28th Annu. Conf. Ind. Electron. Soc.*, Seville, Spain, Nov. 2002, pp. 674–679, doi: 10.1109/IECON.2002.1187588.

[28] D. Schröder, *Elektrische Antriebe—Regelung Antriebssystemen*. Berlin, Germany: Springer, 2015.

[29] F. De Belie and J. Melkebeek, "Seamless integration of a low-speed position estimator for IPMSM in a current-controlled voltage-source inverter," in *Proc. 1st Symp. Sensorless Control Electr. Drives*, Jul. 2010, pp. 50–55, doi: 10.1109/SLED.2010.5542804.

[30] D. Paulus, P. Landsmann, and R. Kennel, "Sensorless field-oriented control for permanent magnet synchronous machines with an arbitrary injection scheme and direct angle calculation," in *Proc. Symp. Sensorless Control Electr. Drives*, Sep. 2011, pp. 41–46, doi: 10.1109/SLED.2011.6051543.

[31] D. Paulus, "Beliebige Injektion für permanent erregte synchronmaschinen arbitrary injection for permanent magnet excited synchronous machines," Ph.D. dissertation, Dept. Elect. Eng. Inf. Technol., Tech. Univ. Munich, Munich, Germany, 2015.

[32] D. Paulus, P. Landsmann, and R. Kennel, "General arbitrary injection approach for synchronous machines," in *Proc. IEEE Int. Symp. Sensorless Control Electr. Drives Predictive Control Electr. Drives Power Electron.*, Oct. 2013, pp. 1–6, doi: 10.1109/SLED-PRECEDE.2013.6684509.

[33] P. Landsmann, C. M. Hackl, and R. Kennel, "Eliminating all machine parameters in encoderless predictive torque control without signal injection," in *Proc. IEEE Int. Electric Mach. Drives Conf. (IEMDC)*, May 2011, pp. 1259–1264.

[34] P. Landsmann and R. Kennel, "Saliency-based sensorless predictive torque control with reduced torque ripple," *IEEE Trans. Power Electron.*, vol. 27, no. 10, pp. 4311–4320, Oct. 2012.

[35] P. Landsmann, D. Paulus and S. Kühl, "System and method for sensorless control of electric machines using magnetic alignment 'Method and device for controlling a synchronous motor without a position sensor by unique assignment of the admittance or inductivity to the rotor location,'" U.S. Patent DE102 018 006 657 A1, Feb. 20, 2020.

[36] S. Morimoto, K. Kawamoto, M. Sanada, and Y. Takeda, "Sensorless control strategy for salient-pole PMSM based on extended EMF in rotating reference frame," *IEEE Trans. Ind. Appl.*, vol. 38, no. 4, pp. 1054–1061, Jul./Aug. 2002.

[37] S. Morimoto, K. Kawamoto, M. Sanada, and Y. Takeda, "Sensorless control strategy for salient-pole PMSM based on extended EMF in rotating reference frame," in *Proc. Conf. Rec. IEEE Ind. Appl. Conf. 36th IAS Annu. Meeting*, Sep./Oct. 2001, pp. 2637–2644.

[38] K. Kato, M. Tomita, M. Hasegawa, S. Doki, S. Okuma, and S. Kato, "Position and velocity sensorless control of synchronous reluctance motor at low speed using disturbance observer for high-frequency extended EMF," in *Proc. 37th Annu. Conf. IEEE Ind. Electron. Soc. (IECON)*, Nov. 2011, pp. 1971–1976.

[39] A. Makimura, Y. Nomura, S. Kondo, and M. Tomita, "Study of influence of inductance variation of position sensorless control of SynRM at low speeds by estimating high-frequency extended EMF caused by superimposed current," in *Proc. IEEE 2nd Annu. Southern Power Electron. Conf. (SPEC)*, Dec. 2016, pp. 1–6, doi: 10.1109/SPEC.2016.7846065.

[40] D. Paulus, J. Stumper, and R. Kennel, "Sensorless control of synchronous machines based on direct speed and position estimation in polar stator-current coordinates," *IEEE Trans. Power Electron.*, vol. 28, no. 5, pp. 2503–2513, May 2013, doi: 10.1109/TPEL.2012.2211384.

MATTHIAS LAUMANN (Member, IEEE) was born in Darmstadt, Germany, in 1989. He received the B.Eng. and M.Sc. degrees in electrical engineering from the Darmstadt University of Applied Sciences, Germany, in 2014 and 2016, respectively. He is currently working toward the Dr.-Ing. (Ph.D.) degree with the Technical University of Munich, Munich, Germany. He has been a Teaching Fellow at the Darmstadt University of Applied Sciences, since 2016. His main research interests include highly reliable sensor fault-tolerant control algorithms for synchronous machines, including the application of encoderless control, control without current sensors, and control without DC-link voltage sensor.

CHRISTIAN WEINER (Member, IEEE) was born in Germany, in 1971. He received the Diploma degree from the Darmstadt University of Applied Sciences, Darmstadt, in 1994, and the M.Sc. and Ph.D. degrees from the Newcastle University, U.K., in 1995 and 2000, respectively. From 2001 to 2013, he held several positions at Linde Material Handling GmbH, Aschaffenburg, Germany. In 2013, he was appointed as a Professor of electric mobility and electric drives at the Darmstadt University of Applied Sciences, Darmstadt, Germany. His research interests include the field of power electronics and drives for mobile applications.

RALPH M. KENNEL (Senior Member, IEEE) was born in Kaiserslautern, Germany, in 1955. He received the Diploma and Dr.-Ing. (Ph.D.) degrees in electrical machines and drives from the University of Kaiserslautern, Kaiserslautern, Germany, in 1979 and 1984, respectively. From 1983 to 1999, he held several positions with Robert Bosch GmbH, Stuttgart, Germany. Until 1997, he was responsible for the development of servo drives. From 1994 to 1999, he was appointed as a Visiting Professor with the Newcastle University, Newcastle upon Tyne, U.K. From 1999 to 2008, he was a Professor in electrical machines and drives with the University of Wuppertal, Wuppertal, Germany. Since 2008, he has been a Professor in electrical drive systems and power electronics with the Technical University of Munich, Munich, Germany. His research interests include renewable energy systems, encoderless control of ac drives, predictive control of power electronics, and hardware-in-the-loop systems. He is a fellow of the IET (former IEE) and a Chartered Engineer in the U.K. In IEEE, he is a Treasurer of the Germany Section as well as the ECCE Global Partnership Chair of the Power Electronics Society. He is an Associate Editor for the IEEE TRANSACTIONS ON POWER ELECTRONICS.

• • •